Sebastian Hofer, BSc

Epitaxial Order of Metal-Organic Frameworks based on Copper and Terephthalic Acid

MASTER'S THESIS

to achieve the university degree of

Diplom-Ingenieur

Master's degree programme: Technical Physics

submitted to

Graz University of Technology

Supervisor

Ao.Univ.-Prof. Dipl.-Ing. Dr.techn., Roland Resel

Institute of Solid State Physics

Graz, April 2018

AFFIDAVIT

I declare that I have authored this thesis independently, that I have not used other than the declared sources/resources, and that I have explicitly indicated all material which has been quoted either literally or by content from the sources used. The text document uploaded to TUGRAZonline is identical to the present master's thesis.

_____
Date

_____
Signature

Acknowledgements

To start I would like to thank my supervisor Roland Resel for making it possible to work in his group and for all the advice he has given me, while working on this thesis. I am very grateful for his continuous support as well as the many helpful explanations he had for me.

Furthermore, I would like to thank Paolo Falcaro and his group, as they allowed me to collaborate closely with them, being able to do my master's thesis in a very interesting and contemporary field. Particularly, I wish to thank Raffaele Ricco, for helping me with all the chemical preparations, which I would not been able to do alone.

I would also like to thank Andrew Jones for supervising my thesis at the beginning, introducing me to all the measurement procedures and helping me interpret my first results.

For the great work experience, I would like to thank all members of the Resel- and the Coclite-group, be it interesting discussions or very determined riddle-solving. I would especially thank Stefan Pachmajer and Benedikt Schrode for being available, whenever questions arose, as well as developing software to allow for convenient data analysis.

Also, I would like to thank the beamline scientists Nicola Demitri and Luisa Barba at the XRD1 beamline at the Elettra Sincrotrone Trieste. Being able to do measurements in their facilities was a great experience.

Finally, I want to thank my parents for their continuous support during all my time studying and for the many years before. Without their assistance, I would have never been able to achieve my goals.

Abstract

Aligned Metal- Organic Frameworks (MOFs) are interesting for usage in optical, sensor and microelectronic application [1]. Recently it is shown that MOFs can be prepared epitaxially on copper hydroxide (Cu(OH)$_2$ [2]. In this work, MOFs, consisting of copper ions, linked in 2 dimensions by 1,4-benzenedioic acid (BDC), as well as 3D-MOFs, consisting of copper, BDC and 1,4-Diazabicyclo[2.2.2]octan (dabco) are grown on Cu(OH)$_2$ nanobelts. The nanobelts with dimensions of several μm in length and 20 nm in width are deposited on silicon surfaces by solution processing. It is apparent that the alignment of the Cu(OH)$_2$ nanobelt substrate is an important parameter for the controlled, oriented growth of MOFs. The epitaxial alignment is studied by X-ray diffraction using pole figure technique as well as grazing incidence X-ray diffraction. The nanobelts are aligned uniaxially with the [100] axis along the silicon surfaces. The MOF follows the orientation of the underlying nanobelts. Interestingly, the formed crystal structures of the MOF cannot be explained by any of the known polymorph phases. Further work must be performed to solve the MOF structure. In a subsequent step a study on the functionalization of grown MOFs by exchanging the ligands is undertaken. Here, an unexpected change in the crystalline structure is detectable, hinting towards a highly anisotropic extension in only one direction.

Kurzfassung

Orientierte Metall-Organische Frameworks (MOFs) sind interessant für ihre Verwendung in optischen, sensorischen und mikroelektronischen Anwendungen [1]. Kürzlich wurde gezeigt, dass es möglich ist, MOFs epitaktisch auf $Cu(OH)_2$ aufwachsen zu lassen [2]. Für diese Arbeit werden MOFs, bestehend aus Kupfer, welche in 2 Dimensionen mittels 1,4-Benzoldicarbonsäure (BDC), als auch solche welche in 3 Dimensionen mittels BDC und 1,4-Diazabicyclo[2.2.2]octan (dabco) verbunden sind, auf $Cu(OH)_2$ Nanogürteln aufgewachsen. Diese Nanogürtel, mit einigen µm Länge und einer Breite von 20 nm, werden mittels Depositionsmethoden aus Lösungen auf Silizium Substrate aufgebracht. Offensichtlich ist, dass die Ausrichtung der $Cu(OH)_2$ Nanogürtel einen wichtigen Parameter für den kontrollierten und orientieren Wuchs von MOFs darstellt. Der Grad der Ausrichtung wird mittels Röntgenmethoden, im Besonderen mittels Röntgenpolfiguren und Röntgendiffraktometrie mit streifendem Einfall, ermittelt. Die Nanogürtel sind uniaxial mit der [100] Achse parallel zur Silizium Oberfläche ausgerichtet. Die MOFs folgen der Orientierung der Nanogürtel. Interessanterweise ist die Kristallstruktur der MOF Kristallite nicht vollständig bekannt. Weiter Arbeit ist zur Lösung der Kristallstruktur notwendig. In einem weiteren Schritt wird eine Studie zur Funktionalisierung der MOFs, durch Austausch der Liganden angestrebt. Hier kann eine unvorhergesehene Änderung der Kristallstruktur beobachtet werden, welche auf eine stark anisotrope Verlängerung in nur eine Richtung hindeutet.

Contents

1. MOF Basics

The following chapter is dedicated to give an overview of Metal-Organic Frameworks as a class of material, their definition, used terminology and structural nomenclature. Furthermore, a quick glance at post-synthesis-modification will be taken

1.1. Definition

A Metal-Organic Framework (MOF) is a porous regular structure, build up from some metallic ions or clusters, which get connected with some organic linker material. Metal clusters are commonly referred to as secondary building units (SBUs) or nodes in MOF context. Figure 1 shows a sketch to visualize the build-up of the framework.
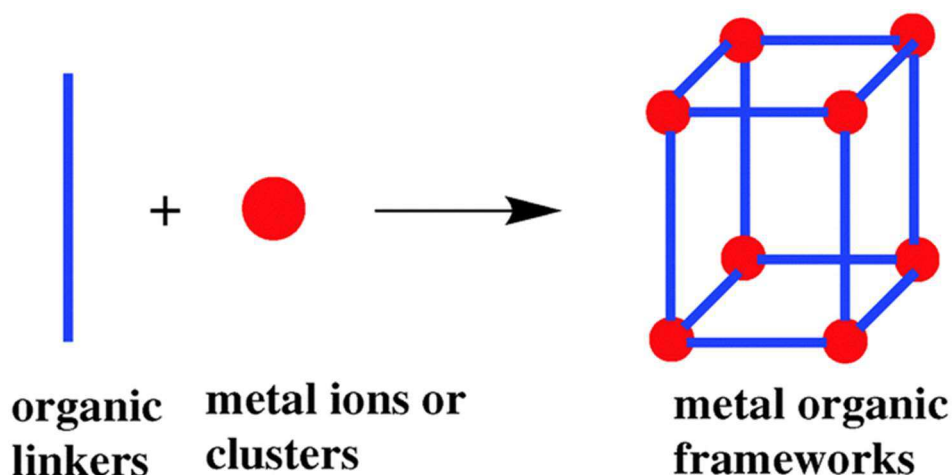

Figure 1 Sketch of the construction of a MOF [3]

Because every metallic cluster and every organic linker can form a MOF, if they bind to each other, there is a high amount of possible combination, resulting in a very diverse class of material. The Cambridge Crystallographic Data Centres (CCDC) database [4], has its own subset of MOF structures with 75.600 entries [5]. The reason for the high number of deposited structures is, that each MOF shows properties, that are precisely tuned by the appropriate metal centres and organic linkers. The linker length, for example, directly changes the size of the pores in the resulting materials, whereas the metal cluster governs the geometry, where the linker attaches to. Furthermore, by adding chemical groups onto the organic linker, one can give specific chemical functionality to the resulting MOF [6], add biomolecules into the large pore space [7] or even add nanoparticles to give e.g. magnetic properties [8] to the MOF material. Possible applications, including, but not limited to specific gas sensing [9], usage as molecular motors [10], bioreactors [11], photovoltaics [12]

and catalysis [13] are currently investigated. Because of this wide-spread possible applications and the very tuneable building-block like approach in material design, there is an increasing academic interest in MOFs. Figure 2 shows the number of publications on MOFs in general and MOFs in the context of device fabrication in the last 20 years.
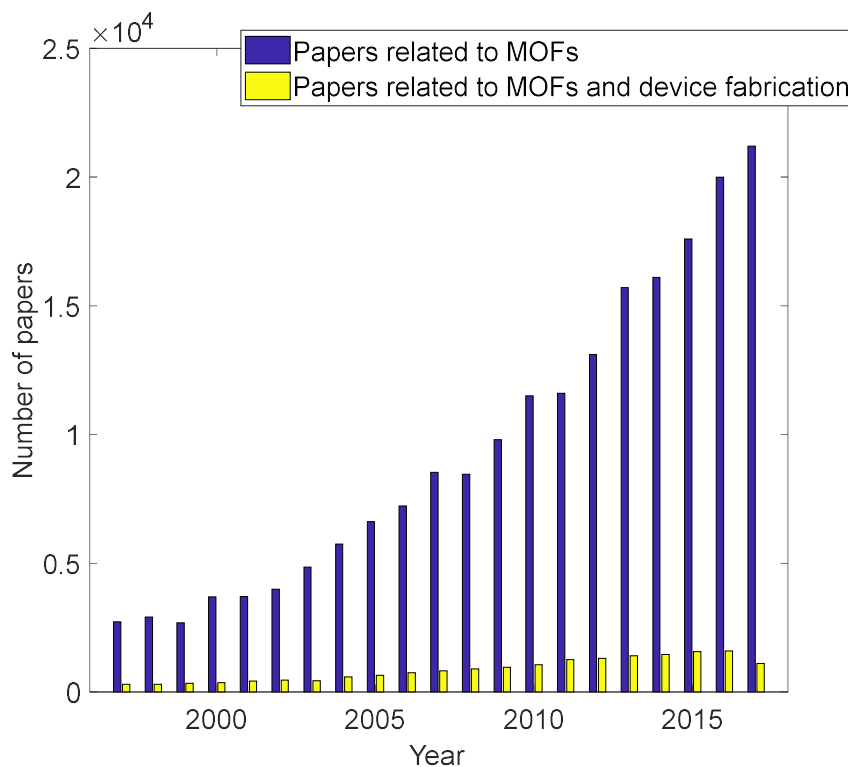

Figure 2 Number of papers related to MOFs and MOF-device fabrication.

In the literature the terms "Metal organic Framework (MOF)", "Microporous coordination polymer (MCP)", "Porous coordination network (PCN)", "Porous coordination polymer (PCP)" and "Zeolite-like metal organic framework (ZMOF)" are used synonymously. For convenience, in this thesis only the term MOF will be used.

Furthermore, because there is no general naming convention for MOFs, different institutes developed their own naming scheme for the MOFs they prepared. In the literature, some of the names for MOFs, stemming from the group, which worked with them, are ZIF (Zeolitic Imidazolate Frameworks [14]), IRMOF (IsoReticular Metal-Organic Framework [15]), MIL (Matériaux de l'Institut Lavoisier [16]) HKUST (Hong Kong University of Science & Technology [17]), COF (Covalent Organic Frameworks [18]), BAF (BergAkademie Freiberg Framework [19]), MFU (Metal–Organic Framework Ulm University [20]) or TOF (Thorium Organic Framework [21]). Adding a number specifies the exact MOF, ending up with convenient, but less descriptive, names like HKUST-1, instead of $Cu_3(btc)_2(H_2O)_3$ (btc=Benzene-1,3,5-tricarboxylic acid).

To give an overview on the very diverse set of building-block materials for MOFs, Figure 3 and 4 show some frequently encountered metal nodes and organic linkers used for MOF synthesis.

Because of the large number of resulting structures and geometries, as well as the inconsistent naming conventions, the next chapter is dedicated to describing the structure of MOFs more generally.
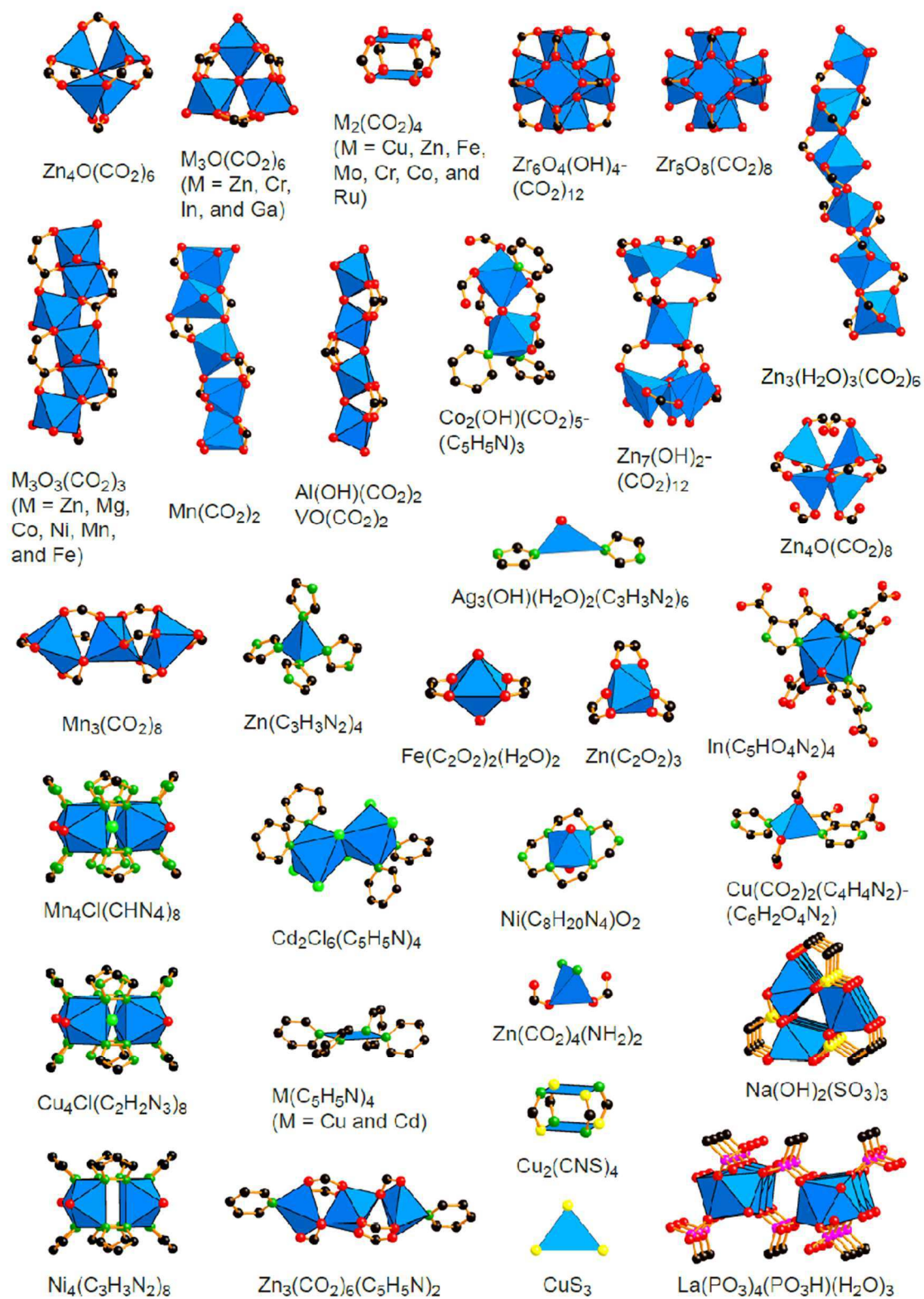
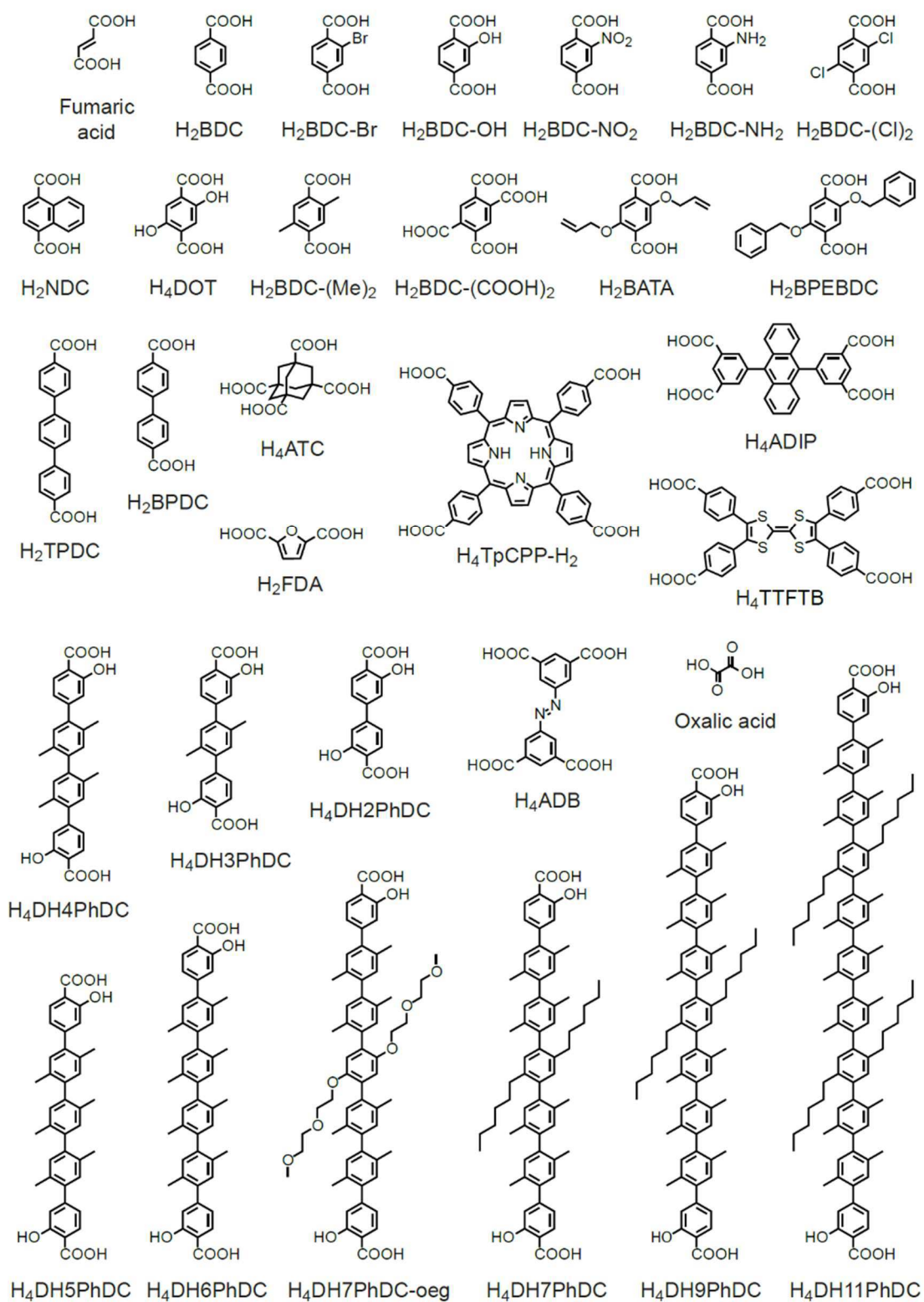*Figure 3 Set of different metal nodes, used in MOF synthesis* [22]

Figure 4 Set of different organic linkers, used in MOF synthesis.[22]

1.1. Structure of MOFs

The structural classification of MOFs is different to ordinary crystalline solids as the view of the material as a regular periodic network is in the foreground, i.e. a topological classification based on a special kind of mathematical graph is used. In this picture there are nodes or vertices which are connected by lines or edges forming a graph. The study of topological networks in the context of chemistry is known as *reticular chemistry* [23] and is used to describe the structure of materials, where the overall topology is more in the focus then the individual bonding of atoms. This helps to define the volume of empty space more intuitively, as it is very important in MOFs. The rigorous basis of defining crystal structure in terms of net and graphs would need a certain firmness in algebraic topology and graph theory and is thus not the scope of this thesis. Instead a general overview should be given, making the reader aware of the nuances one must face, when dealing with networked materials.

The deconstruction of MOFs, as the process of reducing the structure to its topological form is called, tries to describe the metallic nodes as polygons or polyhedral, whose corners act as connection point for other entities (the organic linkers in the case of MOFs). The linker itself is simplified to a line, with a certain number of branches, called the linkers *topicity*. A ditopic linker would in this simplification be reduced to an edge that can connect to two other entities. With those reductions, one can describe any network structure by giving relations between polyhedrons, connected by edges. This helps in classifying networks. Although linker and node sizes may be different, if the same overall geometry is conserved, different materials can be described by the same network topology; they are called *isoreticular*. Unfortunately, there is no general nomenclature to describe those topological nets and different standards are used interchangeably. A short overview on different topological descriptions of nets will be given, serving not as a full explanation, but acting as a hint towards the encountered complexity, when describing topological concepts.

One way of describing a certain net is the so called *Schläfli symbol*. It's a concept from mathematics, useful in the description of tilings [24]. It is a notation of the form {p,q,r,…} to describe any regular polytope. One starts with {p}, which describes a regular polygon with p sides, i.e. {3} would describe a triangle, {4} would describe a square and so on. The second index in the Schläfli symbol, describes how many p-sided polygon facets are around each vertex, e.g. the cube consists of 3 square faces around each vertex and would thus get the Schläfli symbol {4,3}. This can be generalised to more dimensions, yielding a measure

to describe any regular polytopic structure with a set of numbers. Additional to Schläfli symbols there are many more different systems of describing regular structures with a set of numbers, but going into detail on each of them would be outside the scope of this thesis. The most popular ones are vertex symbols, point symbols and face symbols [24] as well as RCSR symbols, the latter one being the used symbol in the Reticular Chemistry Structure Resource (RCSR) database [25].

The reason, why one uses this very abstract description of net topologies is the fact that very complicated metal centre geometries can be described easily. Figure 5 shows sketches for some metallic nodes, and their reduction to a regular polyhedron.
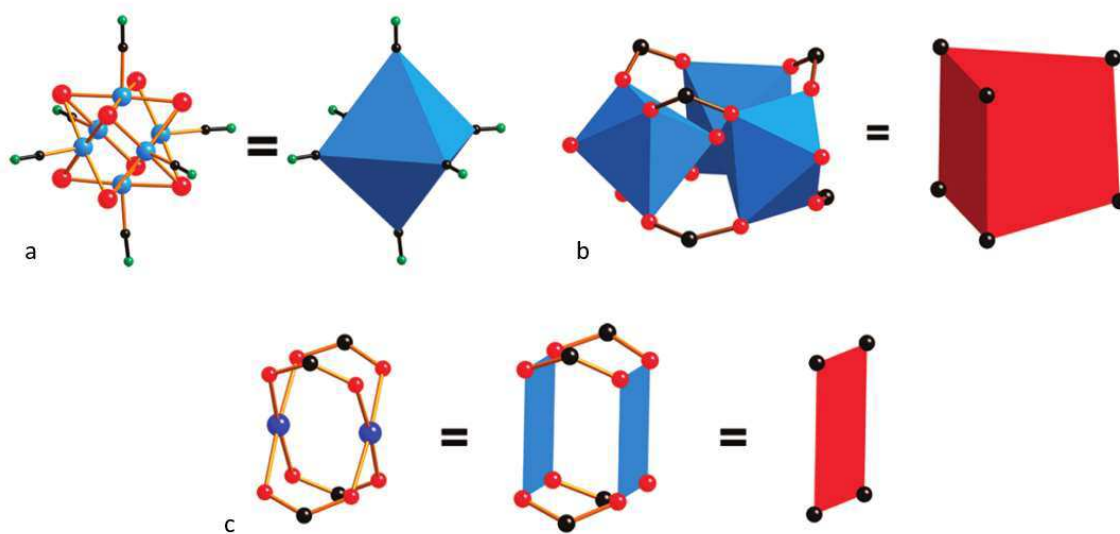

Figure 5 Metallic SBUs and their reduction to a regular polyhedron. a: $Re_6Se_8(CN)_6$, b: $OCr_3(CO_2)X_3$, c: $Cu(SO_4)$. [26]

When reduced to regular polyhedrons, the individual atomic arrangement is not important and all geometric considerations can be done in this simplified form. Analogous simplification for the organic linker is schematically shown in Figure 6.
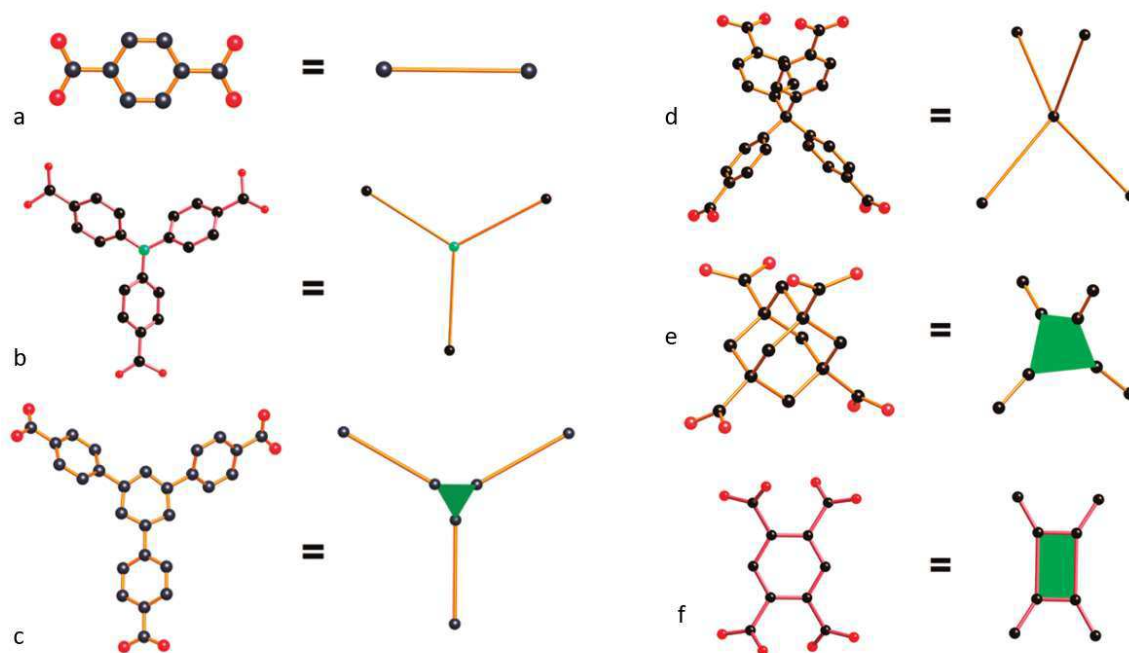
Figure 6 Organic linkers and their reduction to nodes and polyhedrons and nodes respectively. a: Ditopic, b,c: Tritopic, d,e,f: Tetratopic. [26]

Having undergone the reduction of the atomic structure to a set of polyhedrons or nodes one can identify networks with similar structure, even though their atomic arrangement can be different. One is now left with describing the net topology, where topological similarities will yield structural similarities, independent of the involved atoms. Unfortunately, one is still left with many different net topologies, where naming convention is very arbitrary. The RCSR offers a database with 2809 different net topologies in three dimensions. A net identifier in the RCSR is a combination of 3 letters, with the possibility of adding a fourth letter with a hyphen to describe certain modifiers. The names mostly orient themselves on natural minerals that show a similar structure. Examples would be "cor" for the corundum (Al_2O_3) net, or "nbo", as the net of niobium oxide. The primitive cubic net would get the identifier "pcu", whereas a face-centred cubic net would be described by "pcu-b". The whole naming convention is rather cumbersome, but software tools were developed to reduce structures into their underlying nets and look them up in databases. Example of software like this is *Systre* [27].

The two most often encountered net topologies in MOF literature are the "pcu" (primitive cubic lattice) and the "dia" (diamond) net. Figure 7 shows the two nets.
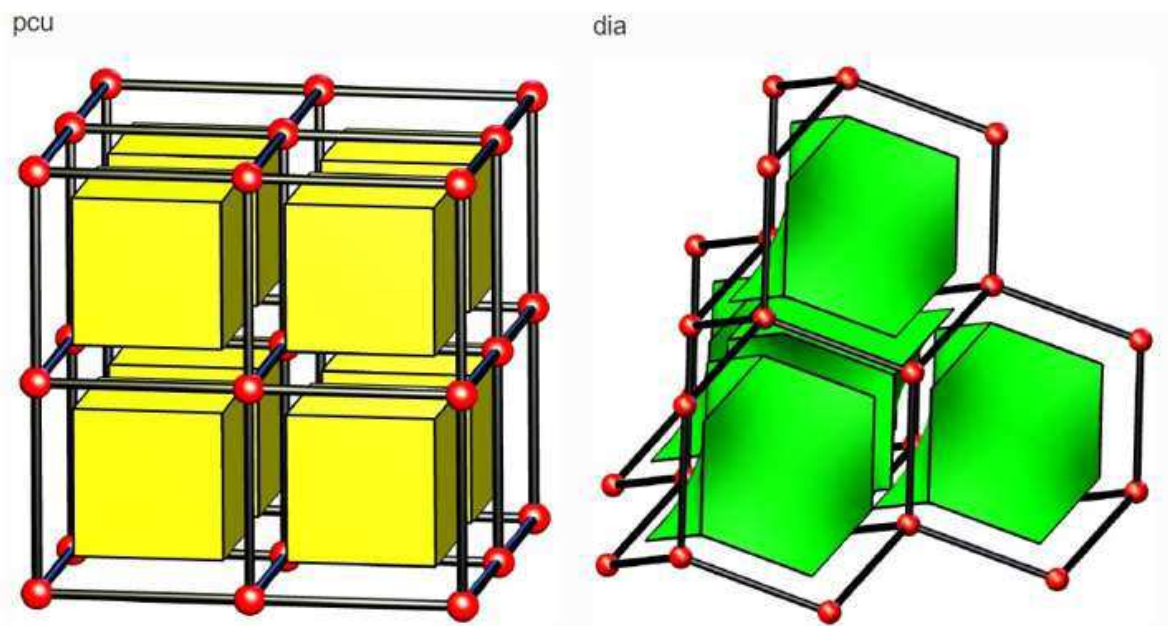
Figure 7 Sketch of the pcu and the dia net, as shown in the RCSR database [25]

One advantage of the deconstruction of the network into topological units is the fact that the large volume of free space can be visualized more easily this way. Because MOFs are highly porous, the holes in the material are very interesting, as they introduce the remarkably high internal surface area into MOFs. Figure 8 shows the deconstruction of a metallic node and an organic linker into their topological equivalents and the resulting net, indicating the empty space with yellow spheres.
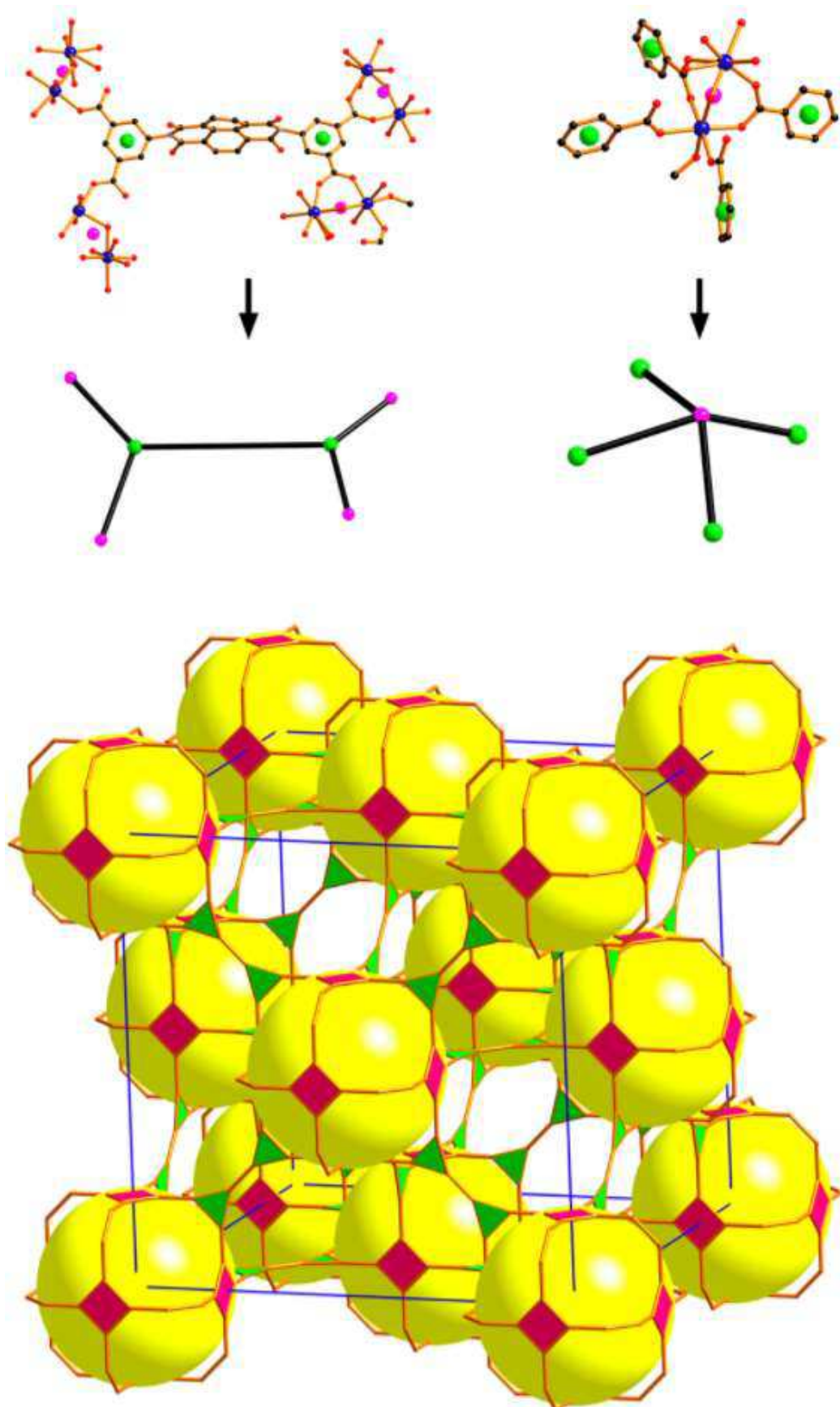
Figure 8 Metallic nodes and linkers of MOF-1 in topological representation (RCSR symbol: tfb-a) , indicating the volume of free space. [26]

It is visible that, by going to a topological description of nets instead of individual atomic arrangement, a material can be described more intuitively, when the focus is on the empty space inside the pores. In the example in Figure 8 above, the spheres, which indicate empty space, are in cubic close-packed geometry, whereas the packing of the individual atoms is much more difficult to describe.

1.2. Ligand Exchange

Ligand exchange describes the replacement of a MOFs organic ligand by another one, after the material has been prepared. If also the metallic nodes in a MOF are replaced by the appropriate chemistry, one more generally calls the exchange reaction post-synthetic modification. Figure 9 shows a sketch on the possibilities in post-synthetic modification of MOFs.
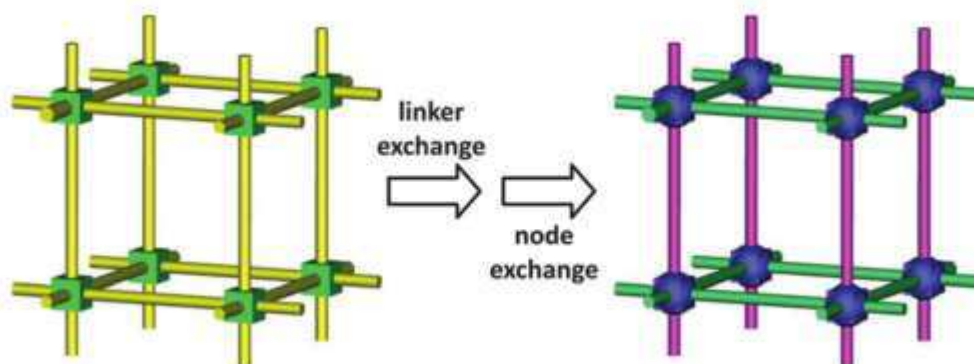

Figure 9 Schematic on the possibilities of post-synthetic modifications in MOFs. [28]

One reason, why the idea of being able to exchange e.g. the linker by some chemically functionalized one after the synthesis, is that the direct growth with the functionalized linker may be not possible. This is because most MOFs are prepared by solvothermal methods, where the chemically active group could be unstable at those temperatures, influence the solubility or bind metallic centres itself, disabling the proper MOF growth [29]. The ability to add precisely defined chemical functionality to an already grown MOF is one example for the very diverse possible application of MOFs. The exchange can be either reversible or irreversible, depending on the individual chemistry of the involved molecules [30]. Very diverse ligand exchange reactions, with conversion efficiencies >70 % of all linkers per conversion cycle were reported [31]. The crystallinity of the material after ligand exchange is generally conserved [29].

2. Methods

In the following chapters an introduction to the experimental methods used, will be given.

2.1. Basic principle of X-ray Diffraction

The basic principle on how to get information on crystallographic features from X-ray diffraction is visible in Braggs Equation [32]. To understand, where it comes from in Figure 10 the geometrical principle is shown.
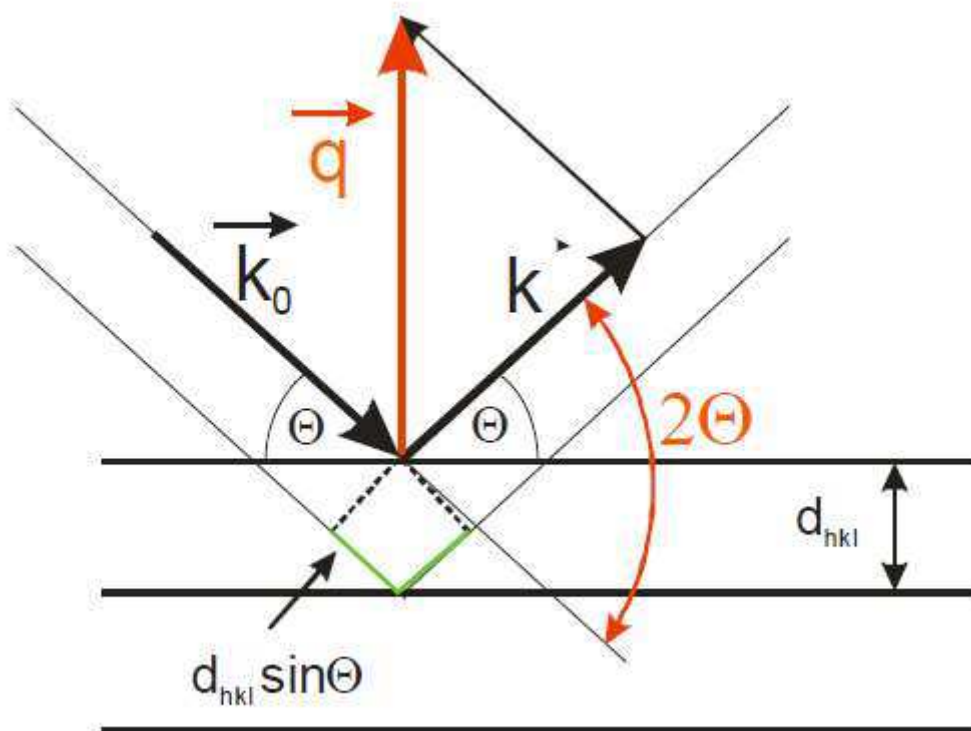

Figure 10 Geometrical perspective on the scattering condition.

An incoming beam gets reflected at atoms in a crystal lattice, with lattice planes being a distance of d_{hkl} apart. Another beam that hits an atom in a lattice plane below will thus travel an additional distance of $2\,d_{hkl}\sin(\Theta)$. If the distance in the way travelled is now an integer multiple of the wavelength (λ) of the beam it can interfere constructively with all the other beams and an intense reflected beam can be measured. So formally, a peak in intensity will be measured if

$$n\lambda = 2\,d_{hkl}\sin(\theta) \tag{1}$$

X-ray diffraction now uses this principle, by using X-rays of a specific wavelength and changing the angle θ over a certain range and measuring the intensity of the reflected beam. By doing this the distances in the crystal lattice can be derived from the position of diffraction maxima.

The same principle, viewed in reciprocal space, is visible in Laue's condition for diffraction [33]. A vector $\vec{q}$, called scattering vector, is defined as the difference between incoming and outgoing wave vector:

$$\vec{q} = \vec{k_0} - \vec{k'} \tag{2}$$

For the case of elastic scattering ($|\vec{k_0}| = |\vec{k'}| = \frac{2\pi}{\lambda}$), the length of the scattering vector can be determined as:

$$|\vec{q}| = q = \frac{4\pi}{\lambda}\sin(\frac{2\theta}{2}) \tag{3}$$

, resulting in a measure, independent of the used wavelength.

Diffraction can occur, if the scattering vector equals a reciprocal lattice vector $\vec{G}$. So formally the analogous condition for diffraction in reciprocal space can be written very shortly as:

$$\vec{q} = \vec{G} \tag{4}$$

2.2. Specular X-ray Diffraction (XRD)

Specular X-ray Diffraction (XRD) is a widely employed method of characterizing crystalline materials. Here, the scattering vector is perpendicular to the sample surface, resulting in information only from lattice planes, which are parallel to the sample surface (out-of-plane). Interplanar distances in other directions (in-plane) cannot be measured this way. The advantage of XRD is, that measurements can be done very quickly and a preliminary material characterisation can be easily done this way.

2.2.1 In-House Setup

Experiments on specular XRD, in-house, are done with a PANalytical Empyrean X-ray diffractometer. Figure 11 shows the components of the experimental setup.
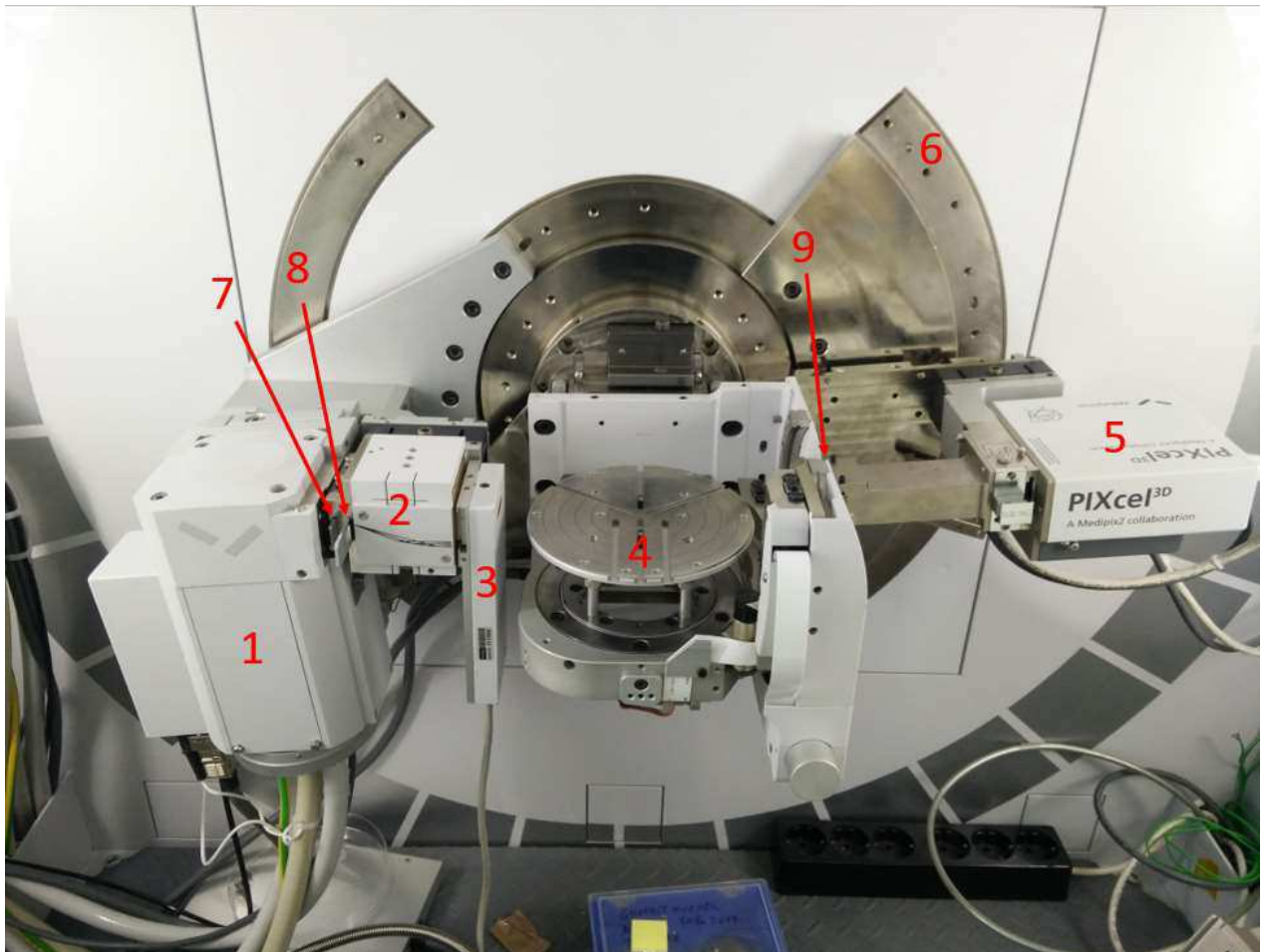

Figure 11 Measurement chamber of the PANalytical Empyrean X-ray diffractometer with indications of the components.

The components are as follows:

1: X-ray Source: X-ray tube, emitting Cu-Kα radiation at λ=1.54056 Å, operated at 40 kV voltage and 40 mA current.

2: Parallel beam mirror: X-ray mirror to parallelize the incident X-ray beams.

3: Beam attenuator: Electrically switched attenuator to limit beam intensity on the detector. Will switch, when the intensity surpasses 900000 counts. Attenuation is done by putting a 0.125 mm Ni-plate, with a precisely known attenuation coefficient in the beams path, and calculating back the original intensity.

4: Sample table: Table, to put the sample on. The table can be moved, rotated and tilted via control software.

5: X-ray detector: *PANalytical PIXcel* Solid State Detector. The number of measuring channels can be changed in the control software, allowing configuration to act as a scanning point-, as well as a line-detector.

6: Goniometer: Motors, to move the incident beam arm and the detector arm, to precisely defined angles with an accuracy of 0.0001°.

7: Divergence slit: Limits beam divergence. Choose between 1/8° and 1/32°.

8: Beam Mask: Sets the width of the X-ray beam. Choose between 4 mm, 10 mm or 20 mm.

9: Anti-Scatter Slit: Reduces signal from scattered X-rays. Choose between 0.1 mm and 7.5 mm.

2.3. X-ray pole figures

X-Ray pole figures are a technique to study texture and preferential alignment in crystalline samples.

2.3.1 Basics

When measuring pole figures, one sets the source and the detector at a specific angle, where one would expect to measure a diffraction peak. This fixes the length of the q-vector. The sample is then rotated (ϕ) and tilted (ψ) on the sample stage. Doing this, all the individual crystallites, whose lattice spacing corresponds to the length of the q-vector, will at one point be brought into scattering condition. The intensity is measured as a function of the rotation and the tilt of the sample. Figure 12 schematically shows the principle of measuring pole figures.
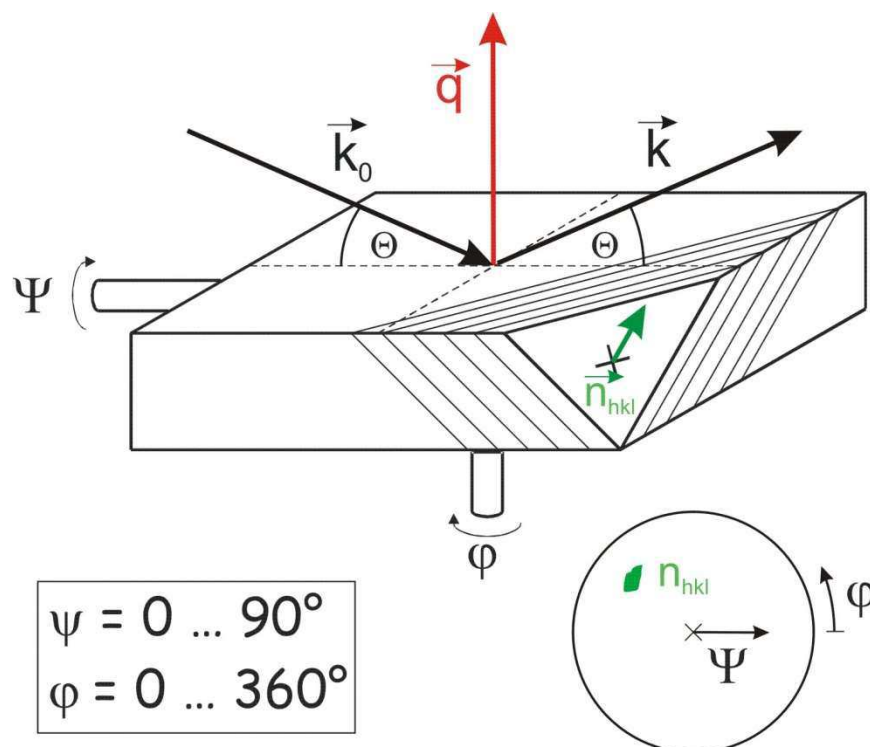

Figure 12 Basic principle on the measurement of X-ray pole figures. The vector $\vec{n}_{hkl}$ gets rotated and turned during the measurement. If at some point it is parallel to $\vec{q}$ diffraction will occur and the diffracted intensity is measured as a function of φ and ψ. [34]

For a powder, a pole figure measurement would result in a constant intensity, whereas textured samples would show characteristic patterns. In Figure 13 one can see a crystallite and the different crystallographic directions present.
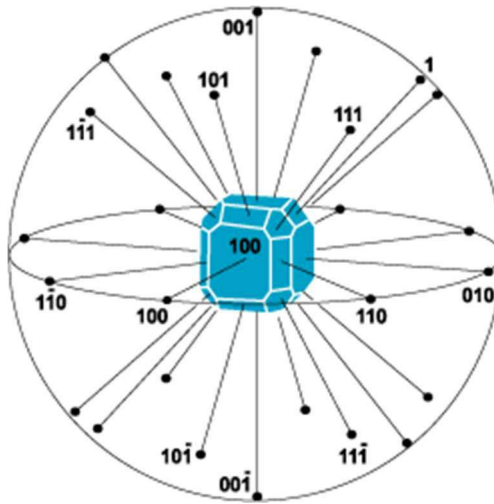
Figure 13 Scheme of a crystallite and indication of different crystallographic direction [35]

To reduce this 3-dimensional map of all the directions to a 2-dimensional map, one uses a method called stereographic projections. Looking from one pole of the sphere, all the directions get projected onto a circular plane and are labelled accordingly. Figure 14 shows a visualization.
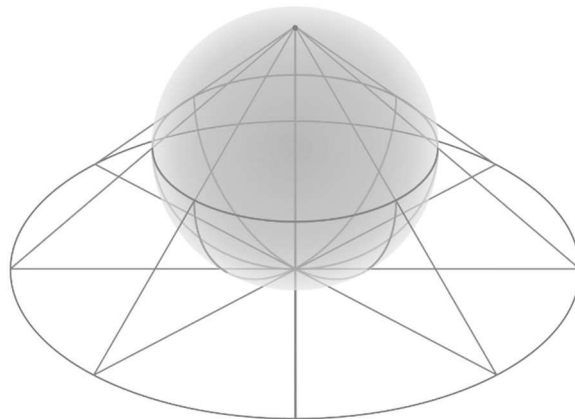

Figure 14 Principle of stereographic projection [36]

By projecting this way, one ends up with a 2-dimenional map where all the independent crystallographic directions are visible. Figure 15 shows an example of such a projection, called Stereogram, for a cubic crystal.
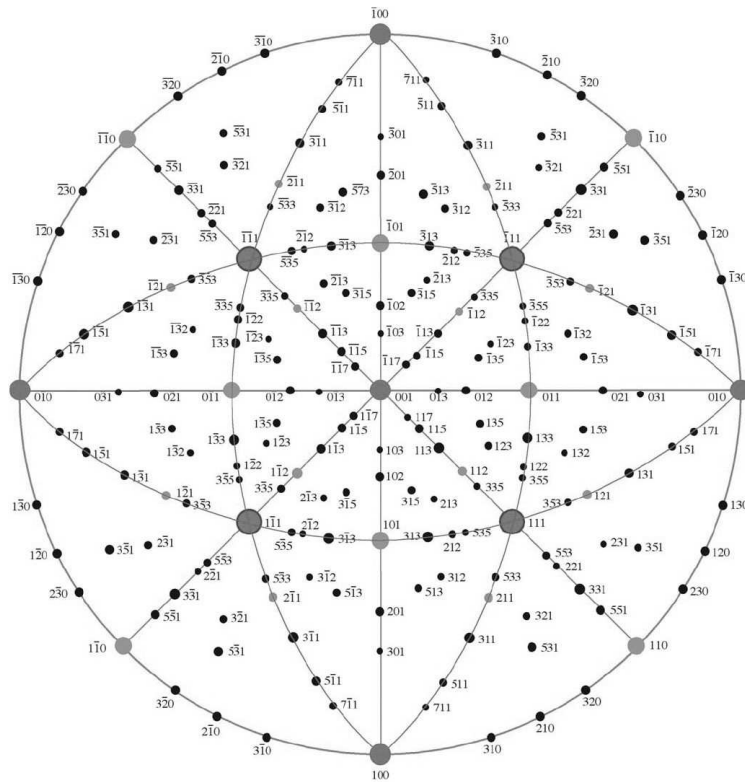
Figure 15 Stereogram for a cubic crystal with labels indicating the net plane normals [37]

The radius in the stereogram corresponds to the samples tilt (0°-90°), while the polar angle corresponds to the rotation of the sample (0°-360°).

2.3.2 In-House Setup

Experiments on X-ray pole figures, in-house, are done with a Philips X'Pert System equipped with an ATC3 cradle diffractometer. Figure 16 shows the components of the experimental setup.

Figure 16 Measurement chamber of the Philips X'Pert System X-ray diffractometer with indications of the components.

The components are as follows:

1: X-ray Source: X-ray tube, emitting Cr-Kα radiation at λ= 2.2897 Å, operated at 40 kV voltage and 30 mA current. Beam area gets chosen by masks at the sources exit and is set to 4 mm height and 2 mm width.

2: Sample table: Table, to fix the sample on. The table can be rotated freely between 0 ° and 360 °, as well as tilted from 0 ° to 90 °.

3: X-ray detector: Point detector, with 1.2 mm slit.

2.4. Grazing Incidence X-Ray Diffraction (GIXD)

GIXD is a method of doing X-Ray diffraction, limiting the signal to coming from surface-near regions.

2.4.1. Basics

The basis of GIXD is using a very small incidence angle in the range of the critical angle of the sample (~0.2°). Below the critical angle, the incoming wave gets totally reflected on the sample and no X-rays enter the material. Instead an evanescent wave on the sample surface is formed, which decays exponentially away from the surface. The diffraction of this evanescent wave with the sample is detected, resulting in a signal coming only from surface layers. Figure 17 shows a schematic picture of a GIXD measurement. The signal is then detected, with a large 2-dimensional detector, resulting in full scattering information, from the projection of the scattering vector in in-plane (q_{xy}) as well as in out-of-plane direction (q_z). To access the angular dependence of the signal, the sample can be rotated on the sample tray.
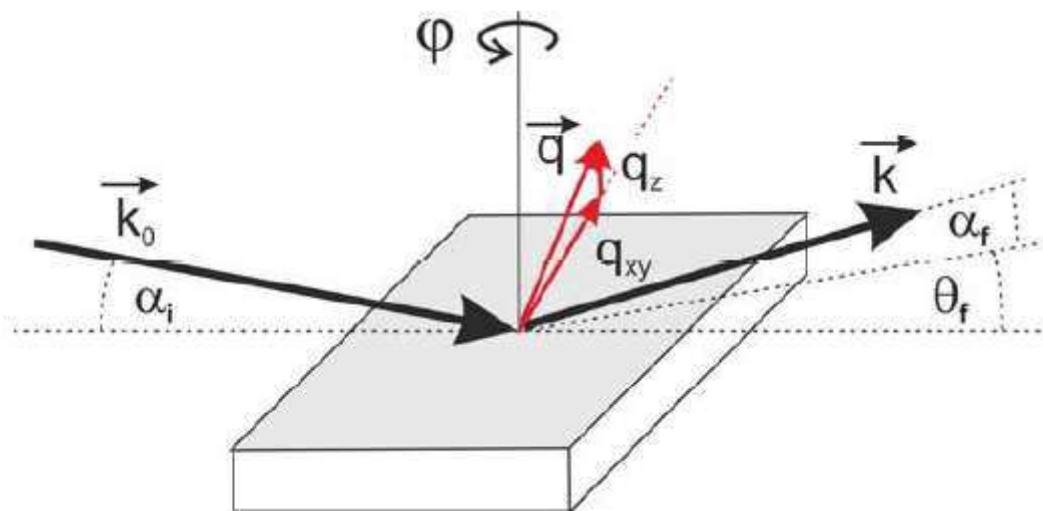

Figure 17 Basic principle of GIXD measurement.[38]

2.4.2 Synchrotron Setup

The synchrotron measurements are performed at the XRD1 beamline at the Elettra synchrotron in Trieste. The detector at the beamline is a Dectris Pilatus 2M detector, allowing to map a large 2-dimensional section of k-space. For details on all the specifications, please refer to Elettra's homepage[39].

2.5. GIXDPF

Grazing Incidence X-ray Diffraction Pole Figures (GIXDPF) is a newly developed method transform GIXD data to the data one would get out of pole figure measurement from GIXD-images. Every pixel in the GIXD-map is located at a position, which is defined by a value of q_z and q_{xy}. Ψ is the angle between q_{xy} and q_z, whereas ϕ is the angle between q_x and q_y. The transformation between $\vec{q}$ and ϕ and ψ is done as follows:

$$\tilde{\psi} = \text{atan}\left(\frac{q_{xy}}{q_z}\right) * \frac{180\,°}{\pi}$$

$$\Phi = \text{atan}\left(\frac{q_y}{q_x}\right) * \frac{180\,°}{\pi}$$

$\widetilde{\Psi}$ is then further transformed via stereographic projection from a pole in the following way, resulting in the same ψ value, one measures in a pole figure:

$$\psi = \cot\left(\frac{180\,° - \tilde{\psi}}{2}\right) * 90\,°$$

This way it is possible to calculate a pole figure signal from GIXD-maps. It is necessary that the sample is rotated during measurement, so the full range of ϕ is accessible. The data analysis is done in *GIDVis*, a MATLab based, GIXD-analysis tool, written by S. Pachmayer and B. Schrode [40].

Because of how the detector is build up, there are certain regions, where no intensity can be measured. Those blind regions result in rings of no intensity in the calculated pole figures.

3. Oriented MOF Approach

The approach to grown oriented MOF crystals, by choosing an oriented substrate as template and source for material is presented here. The method is based on the work of P. Falcaro et. al. [2].

3.1. Idea

MOFs are usually prepared via solution-processing, resulting in a random powder, dispersed in solution. The new idea was to use an oriented substrate on which the MOF crystallites can grow on, epitaxially. Epitaxy, in this context means, that the MOF has a matching unit cell axis with the underlying substrate. Furthermore, the substrate should, at the same time, serve as a reservoir for the metallic nodes, that build up the framework.

The group could find a copper based MOF with unit cell axis, matching those of copper hydroxide ($CuOH_2$). Figure 18 shows the unit cell of copper hydroxide, as well as its unit cell lengths and the unit cell lengths of a MOF, consisting of copper acetate centres, linked with 1,4-Benzenedioic acid (BDC) to 2-dimensional upright-standing sheets.
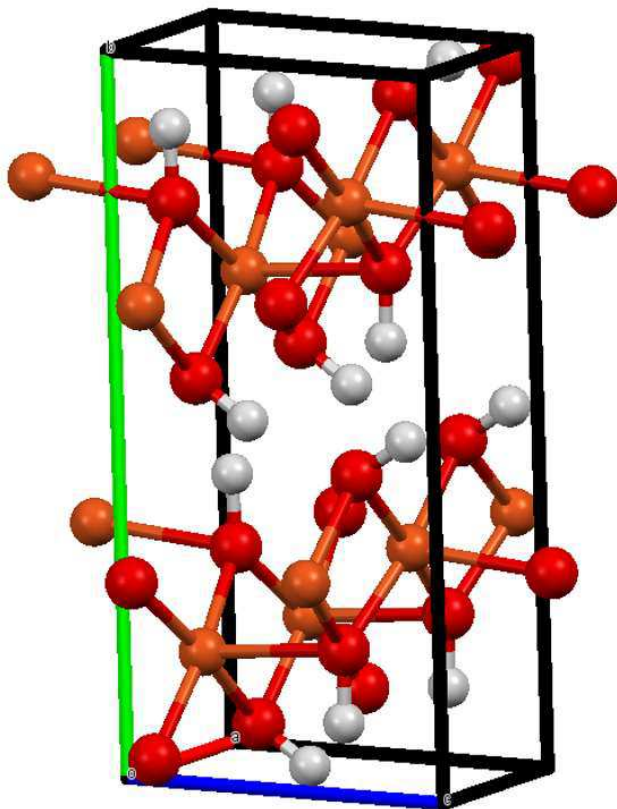
Cu(OH)$_2$	
Space Group	C m c 2$_1$
a	2.95 Å
b	10.59 Å
c	5.26 Å

Cu$_2$(BDC)$_2$	
Space Group	P4
a	5.80 Å
b	10.61 Å
c	10.61 Å

Figure 18 Unit cell of copper hydroxide with unit cell parameters [41] *and proposed unit cell parameters for a copper-based MOF, linked with BDC* [2].

Unit cell length a and c of Cu(OH)$_2$ are very close to an integer multiple of the unit cell lengths a and b of the Cu(BDC)-MOF. This indicates the possibility for epitaxial growth, as the lattice mismatch is below 2%, a rule of thumb for epitaxial lattice matching in the present case [42]. Figure 19 shows a sketch of the Cu(BDC)-MOF and its building blocks.
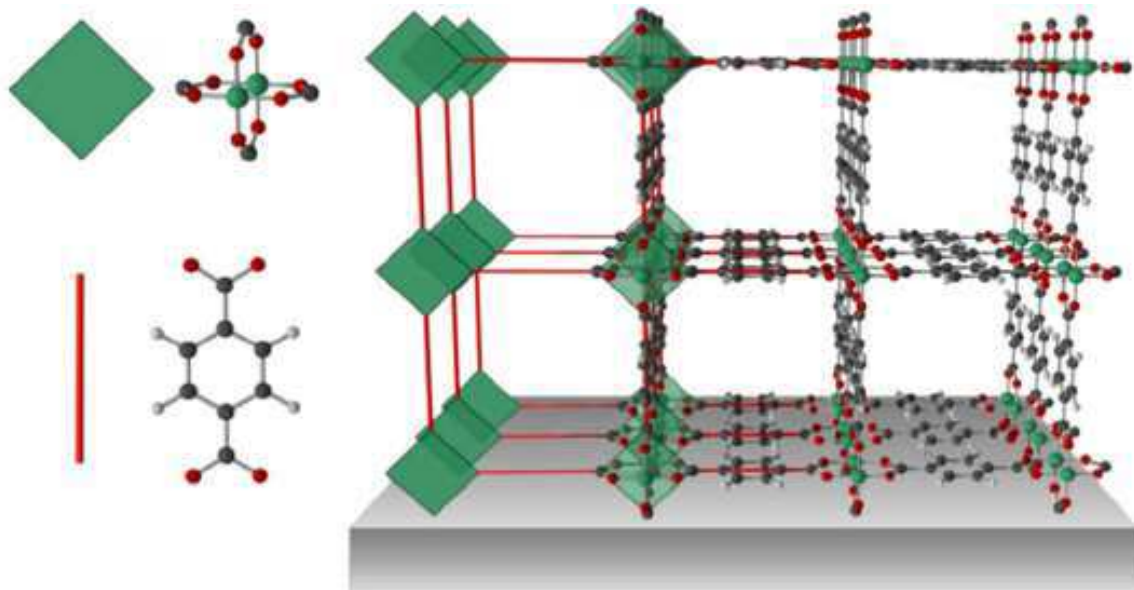
Figure 19 Proposed structure of Cu(BDC)-MOF, showing copper acetate nodes and BDC linker [43]*.*

Viewed from the top, the epitaxial relationship between substrate and MOF is visible. This is shown in Figure 20, indicating the location of copper atoms in the substrate as well as in the MOF and their overlap.
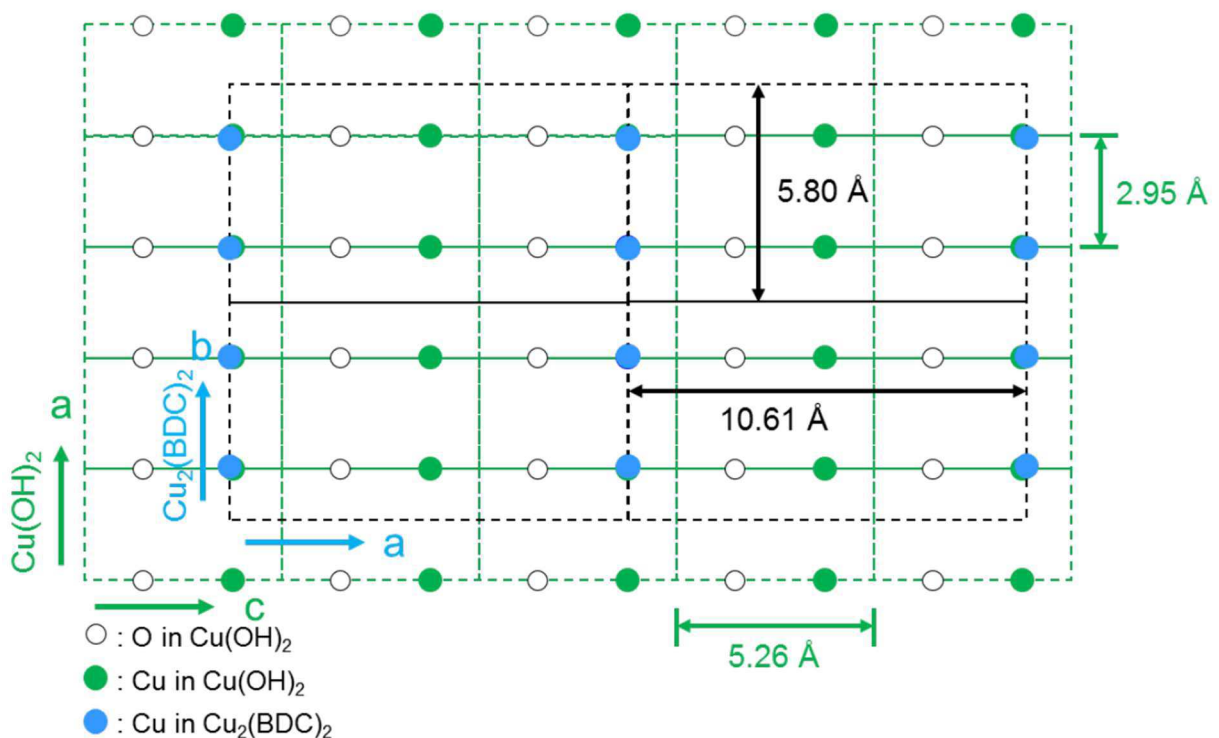

○ : O in Cu(OH)$_2$
● : Cu in Cu(OH)$_2$
● : Cu in Cu$_2$(BDC)$_2$

Figure 20 Proposed epitaxial relationship between copper hydroxide substrate and Cu(BDC)-MOF [2]*.*

Another MOF can be realized in the same way, by further connecting the 2-dimensional sheets with another organic linker of appropriate length. In this case, this additional linker

31

is 1,4-Diazabicyclo[2.2.2]octan (dabco), resulting in the 3-dimensional MOF Cu(BDC)(dabco). Figure 21 shows a sketch to visualize the two different MOFs and how they are linked.
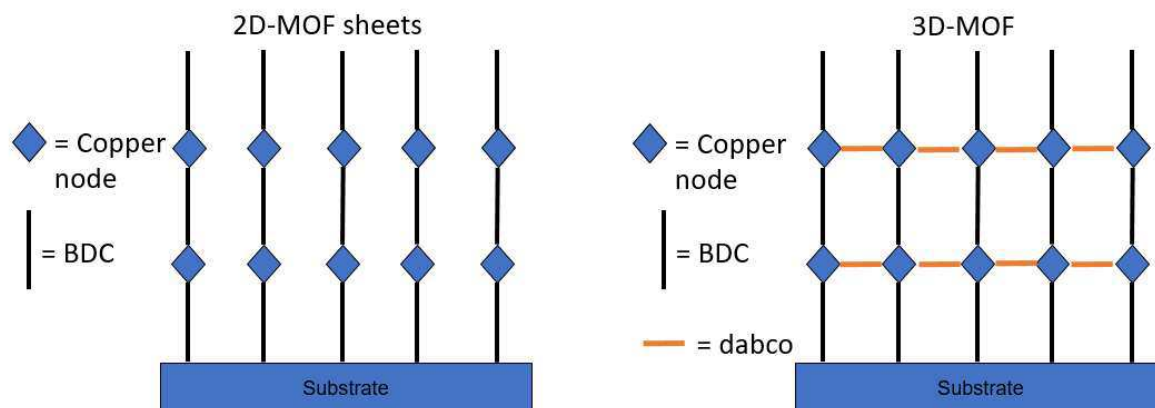

Figure 21 Schematic depiction of the 2-dimensional MOF sheets and the 3-dimensional MOF.

The MOFs, presented above show the possibility to be grown epitaxially on copper hydroxide, because their lattice parameters show only very slight mismatch. By having an oriented copper hydroxide substrate, it therefore would be possible to grow oriented MOFs. The way, this is done, is to prepare very high aspect ratio nanoobjects out of copper hydroxide and orient those. Via solution processing from copper sulphate ($CuSO_4$), µm long and only tens of nm wide, belt-like structures can be produced. In the context of this work, they will be referred to as copper nanobelts. By arranging these nanobelts with some preferred orientation onto a silicon wafer, they can serve as an oriented copper hydroxide substrate. The arrangement of these copper nanobelts is done via a "Langmuir"-inspired method. A solution of copper nanobelts, dispersed in ethanol is carefully ejected from a syringe at a speed of 200 µl/min onto a water reservoir. Because of their high aspect ratio, the individual belts arrange themselves to reduce surface tension. When the whole water surface is covered by the copper nanobelts (visible as a slender film on the water), a silicon wafer is gently dipped at an angle into the water and pulled out swiftly, leaving the nanobelts on the wafer. After cleaning the wafer with ethanol, the alignment of the nanobelts can be studied with light microscopy. Because the procedure is very prone to errors, as it is done by hand, repeated fabrication as well as experience is needed to get highly aligned samples. Figure 22 shows a schematic visualization of the deposition method.
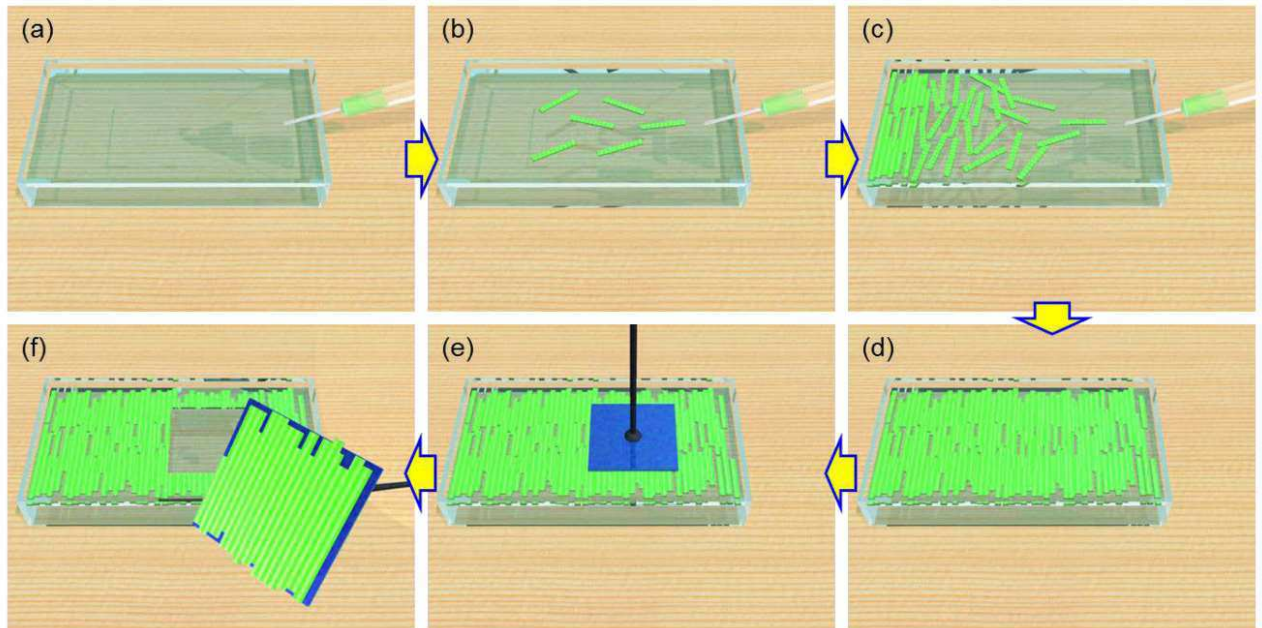
Figure 22 Deposition method for oriented copper nanobelts. [2]

The step of pulling the wafer out of the water is the most critical step in conserving the alignment. For best results, it is advised to push the wafer in very carefully face-down and pull it out in one gradual tilting motion. Using tweezers is not recommended as the tip can disorder the floating nanobelts, if it enters the water surface before the sample.

3.2. Challenges

The most important part in the fabrication of oriented MOFs on copper nanobelt substrate is the alignment of the nanobelts. Depending on the dipping speed, the resulting substrate may be properly aligned or show random orientations. To check for the alignment light microscopy is used. Figure 23 shows an ordered copper nanobelt substrates in light microscopy.
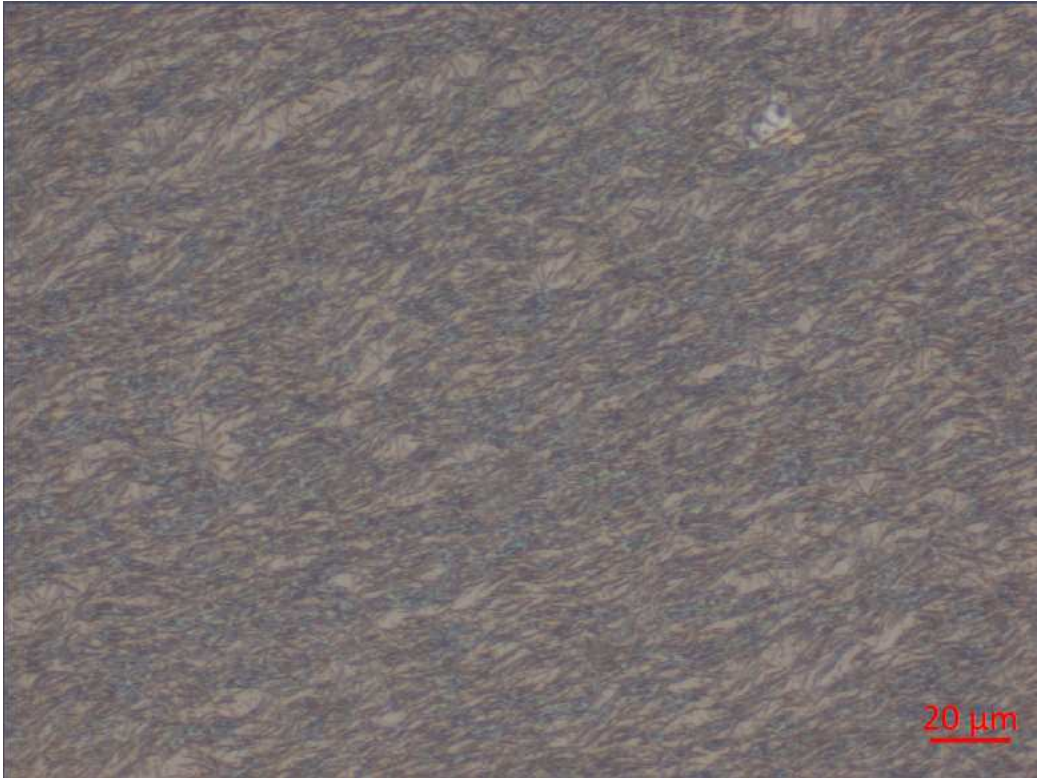
Figure 23 Light microscopy image of oriented copper nanobelt substrate.

In contrast an unsuccessful transfer of the nanobelt onto the wafer yields very disordered nanobelt substrates, depicted in Figure 24.
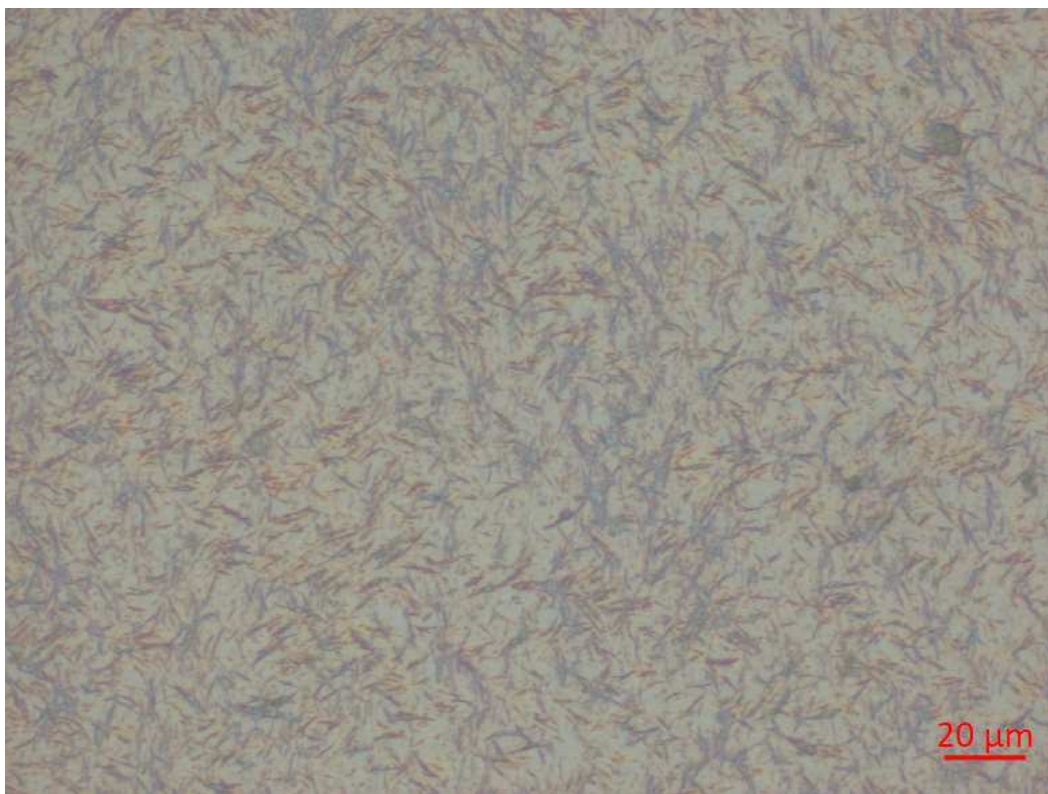

Figure 24 Light microscopy image of randomly oriented copper nanobelt substrate.

4. Preparation Procedures

This section summarizes the preparation recipes for the different materials, as used in the group of Falcaro et al.

4.1. Copper nanobelt preparation

The synthesis of the copper nanobelts starts by dissolving 202 mg of copper(II) sulphate pentahydrate ($CuSO_4 \cdot 5H_2O$) in 20 ml of water, resulting in a 40 mM solution. Additionally, a 150 mM ammonia solution is prepared from 100 µl of 25% ammonia in 5.9 ml of water. The ammonia solution is added dropwise to the copper solution and is then stirred for 5 minutes at 800 rpm. 1.2 ml of 12 M sodium hydroxide solution is added dropwise, changing the colour of the solution from light to dark blue, followed by vigorous stirring for 60 minutes at up to 1250 rpm. The solution is then put in an oven at 40 °C for 30 minutes. As a next step the material gets centrifuged and washed, once with water and twice with ethanol, each centrifuging happening at 4500 rpm for 10 minutes and finally dispersed in 10 ml of ethanol. For details on subsequent deposition, please refer to chapter 3. [44]

4.2. MOF recipes

For the 2-dimensional MOF, a starting solution, consisting of 1 mg 1,4-Benzenedioic acid (BDC) in 7.14 ml ethanol and 2.86 ml water is prepared and sonicated for 5 minutes. For the MOF growth, a wafer, with oriented copper nanobelts is put into the solution and kept there for 10 minutes. Finally, the sample is washed with ethanol and dried in an air stream.

For the 3-dimensional MOF, the starting solution consists of 7 mg terephthalic acid and 4.5 mg 1,4-Diazabicyclo[2.2.2]octan (dabco) in 10 ml methanol. After adding a wafer with oriented copper nanobelts, the solution is put in an oven at 70 °C for 60 minutes. After the synthesis, the wafer is washed with ethanol and dried in an air stream. [2]

4.3. MOF Powder preparation

The MOF powder samples were prepared from the copper nanobelts, disperse in ethanol. To increase the likelihood, that all the copper nanobelts are transformed into MOFs, the molarity of the linker solution was increased 5-fold, resulting in a 10 mg BDC in 14.28 ml ethanol and 5.72 ml water solution for the 2-dimensional MOF and a 70 mg BDC, 45 mg dabco in 20 ml methanol solution for the 3-dimensional MOF. After 10 minutes of

conversion in air and 60 minutes at 70 °C respectively, the resulting MOF powders were washed with ethanol and centrifuged, to remove excess solvent and left to dry.

4.4. Ligand Exchange reaction

For the ligand exchange reaction, the MOFs, prepared by the method described above is put in a 32-mM solution of 2-amino-terephthalic acid (NH_2-BDC) in 10 ml of ethanol. The exchange reaction is done in cycles in an oven at 65 °C for 30 minutes. After each cycle, the sample is cleaned with ethanol and dried. After the 5th cycle, no more change in signal is measured in FTIR, concluding that no more exchange reactions happen.

5. XRD

The first step of characterisation is done via specular XRD. A diffraction pattern on the oriented copper nanobelt substrate is measured for one hour in parallel beam geometry, with a fixed 10 mm beam mask, 1/8° divergence slit, 7.5 mm anti-scatter slit and a 0.02 rad soller slit. The detector serves as a scanning line detector with 255 channels. The resulting measured spectrum is shown in Figure 25.
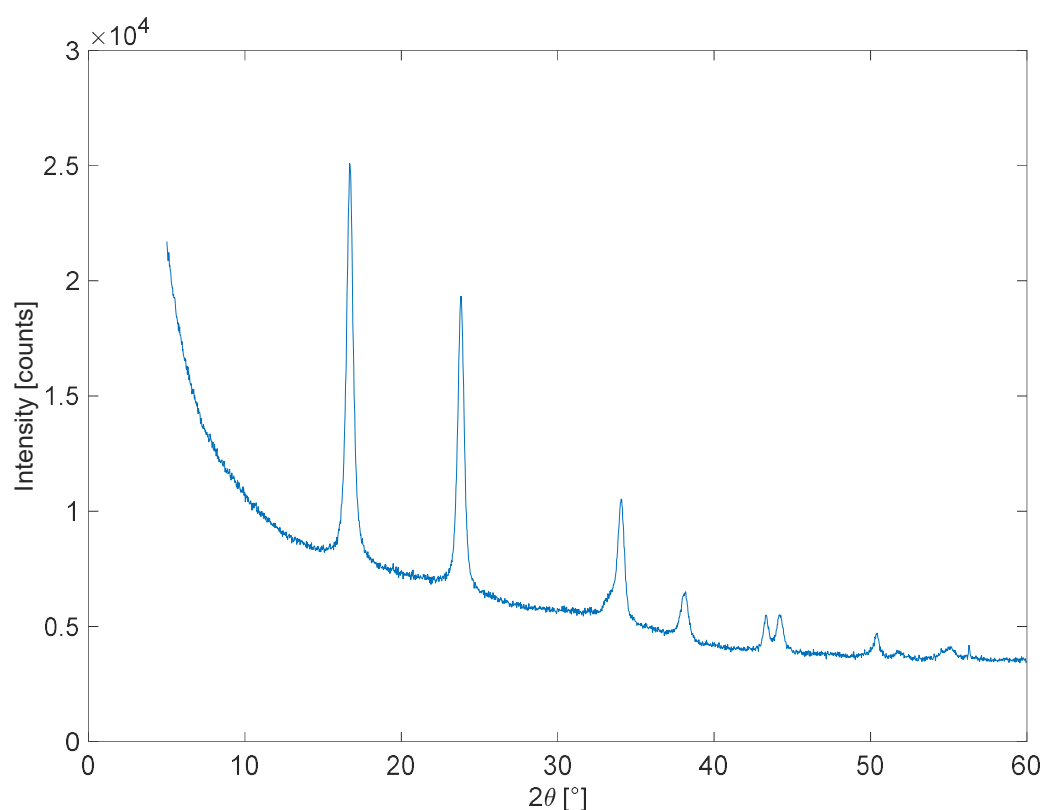

Figure 25 XRD-spectrum of oriented copper nanobelt substrate

For better comparability the following data treatment steps are done. First, the background is removed. This is done via the method of Sonnefeld and Visser [45], implemented in the software tool *HighScore Plus* [46]. Afterwards, the intensity is normalized on the height of the highest peak in the spectrum. For wavelength-independence, the angle is converted to q, following Equation 3. The treated spectrum is then compared to a powder pattern of copper hydroxide, calculated from the crystal structure, deposited by Oswald et al. [41], with the software tool *Mercury* [47]. Figure 26 shows the treated spectrum and a comparison with the calculated powder data.
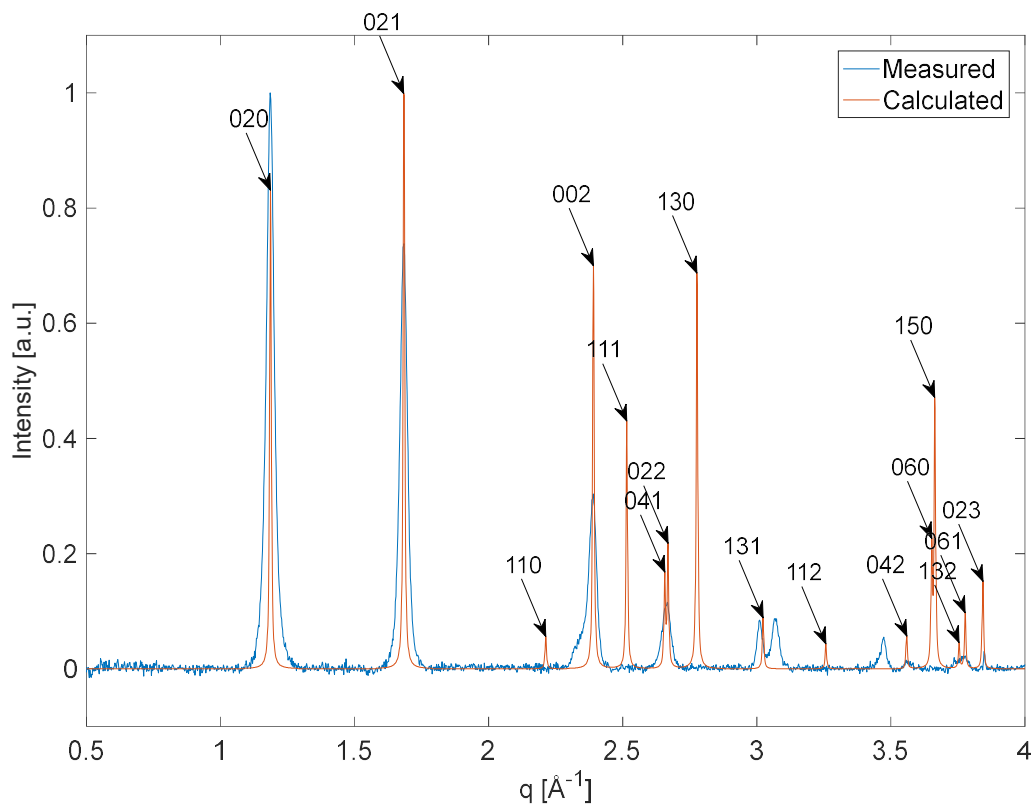
Figure 26 XRD-spectrum of oriented copper nanobelts, after data treatment and comparison with calculated powder data.

Visibly, the peak positions of the calculated spectrum fit very nicely with the measured one, with the complete absence of some calculated peaks. By looking at the missing peaks, one can see that all of them are indexed as hkl with h≠0. The consequence of this is, that the a-axis of $Cu(OH)_2$ is in the direction of the long axis of the copper nanobelts. And because of their high aspect ratio, the belts are expected to lie flat on the substrate, resulting in no crystallites with their a-axis in specular direction. Furthermore, there is an intensity difference, between measured and calculated powder pattern. Because the intensity on the (020) peak is higher, than in a powder, it is apparent that there exists, in fact, a preferential orientation, with the [100] direction parallel to the substrate. Figure 37 shows a sketch of a copper nanobelt, with indications of the crystallographic directions.

Figure 27 Crystallographic directions in copper nanobelts.

In the region between 3 Å^{-1} and 3.5 Å^{-1} there are 3 peaks visible that are not indexed by $Cu(OH)_2$. Two of those peaks can be attributed to the bulk phase of copper, but the peak at q=3.069 could not be indexed. This is shown in Figure 28.
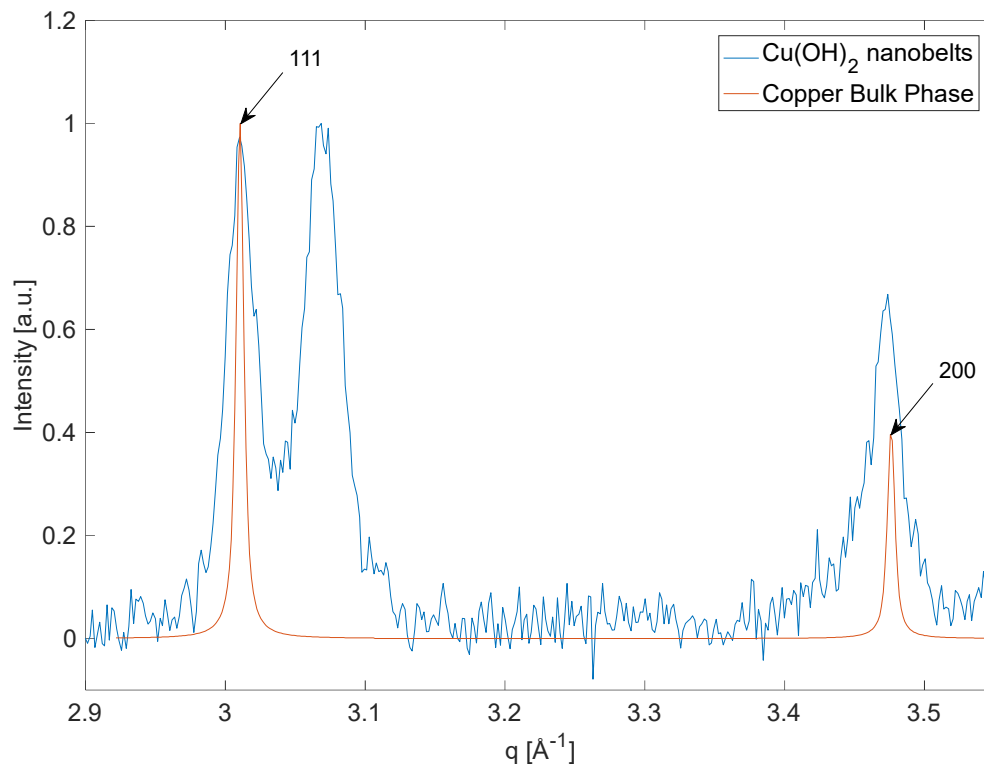

Figure 28 Enlarged section of the diffraction pattern of the copper nanobelt substrate and indexation with copper bulk phase.

On a different sample, the three peaks, shown in Figure 28, could not be found. They appear to come from slightly different preparation conditions between individual substrates.

In a next step, the specular XRD pattern of the 2-dimensional MOF Cu(BDC), is measured and compared with the signal from the nanobelt substrate. The diffraction patterns are shown in Figure 29.
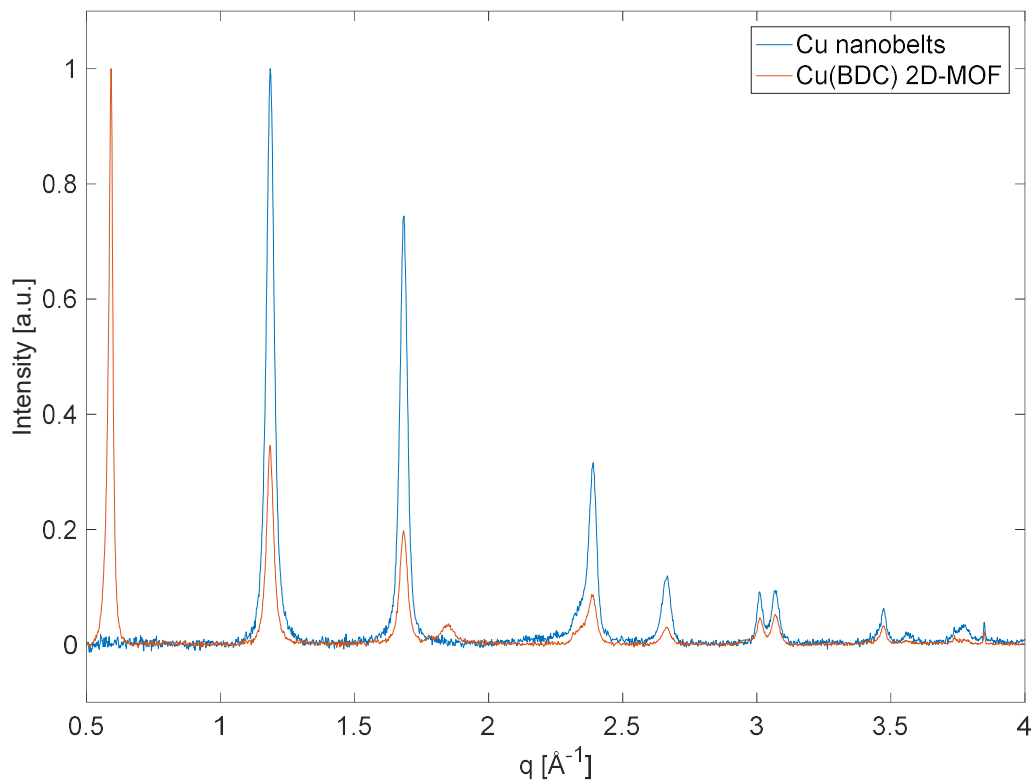

Figure 29 XRD patterns of oriented copper hydroxide nanobelts and 2-dimensional Cu(BDC)-MOF.

One can see the matching of the peaks with the substrate, as is expected due to their epitaxial relationship. The single substrate-independent peak at $q = 0.5932 \, \text{Å}^{-1}$ corresponds to an interlayer distance of $d = 10.592 \, \text{Å}$, matching the reported c-axis length in Cu(BDC) of $c = 10.61 \, \text{Å}$ [2] closely. To gather further information a comparison with calculated powder data, similar as for the copper nanobelt substrate was tried, but did prove unsuccessful, since several different bulk structures of Cu(BDC) are reported, none of which fit the powder pattern from the epitaxial grown MOF. Figure 30 shows a comparison of the measured epitaxial grown Cu(BDC) signal and several reported structures for comparable MOFs, consisting of copper and BDC.
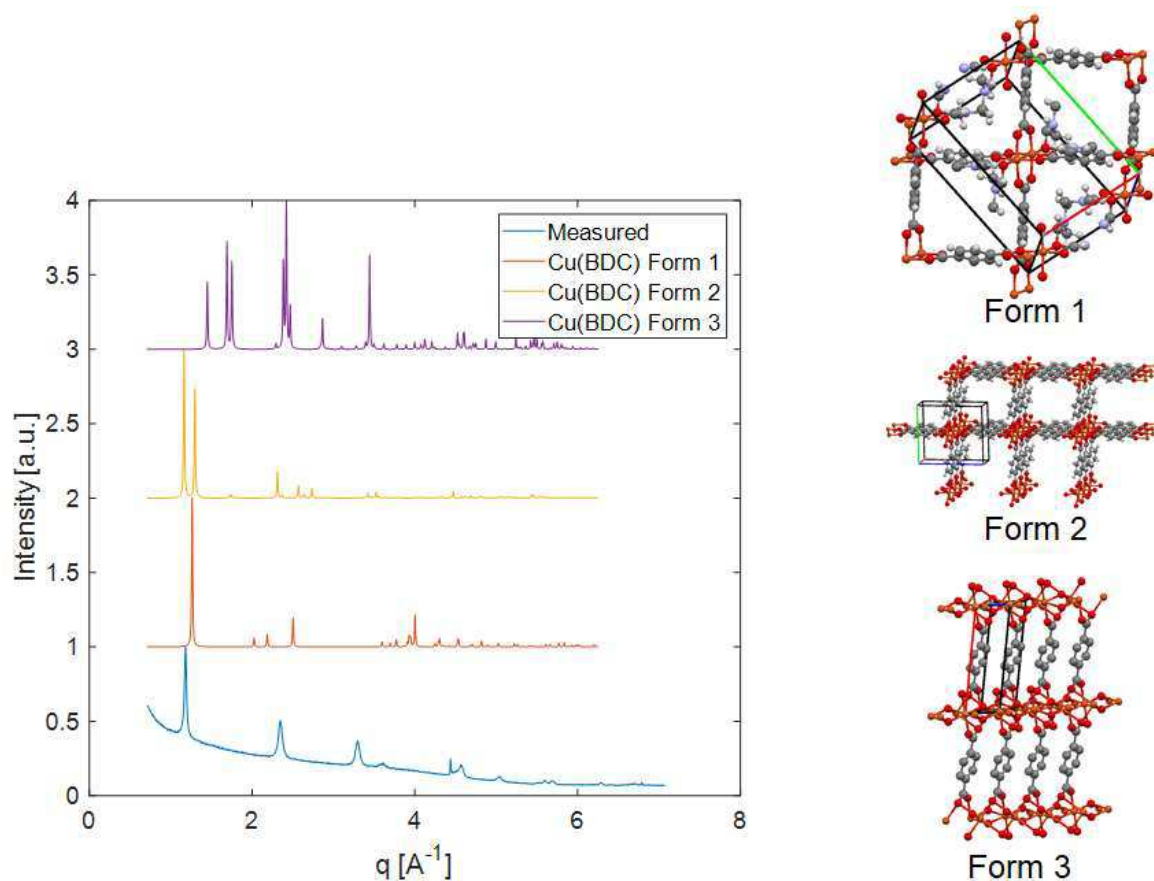
Figure 30 Comparison between measured signal for epitaxially grown 2-dimensional Cu(BDC) MOF on Cu nanobelts and different structural models for MOFs consisting of copper and BDC.

Apparently, none of the reported crystal structures (Form 1 [48], Form 2 [49] or Form 3 [50]) fit the measured signal exactly; an adequate structural model is yet to develop. Because Form 2 fits best to the measured signal, it will be taken as a template for further structural analysis. Figure 31 shows the structure of this Cu(BDC) MOF, reported by Carson et al. [49].
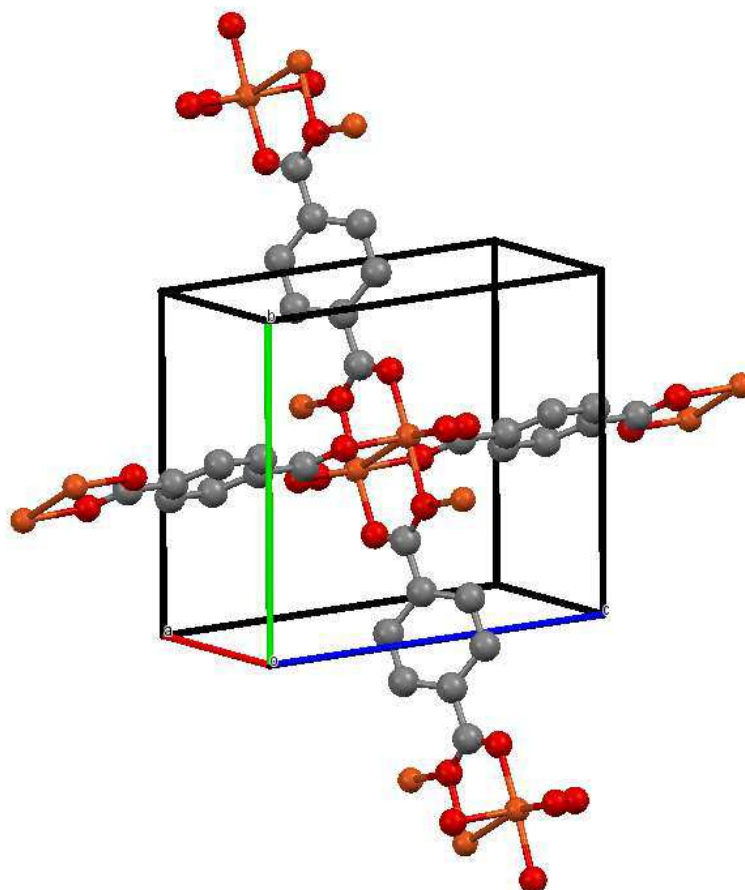
Figure 31 Structural model of a reported Cu(BDC) MOF [49]*, the signal of which fits best to the epitaxially grown one.*

As with the 2-dimensional MOF Cu(BDC), also for the 3-dimensional MOF Cu(BDC)(dabco), specular XRD is measured. The resulting pattern, compared to the patterns of the oriented nanobelt substrate, as well as to the 2-dimensional MOF is visible in Figure 32.
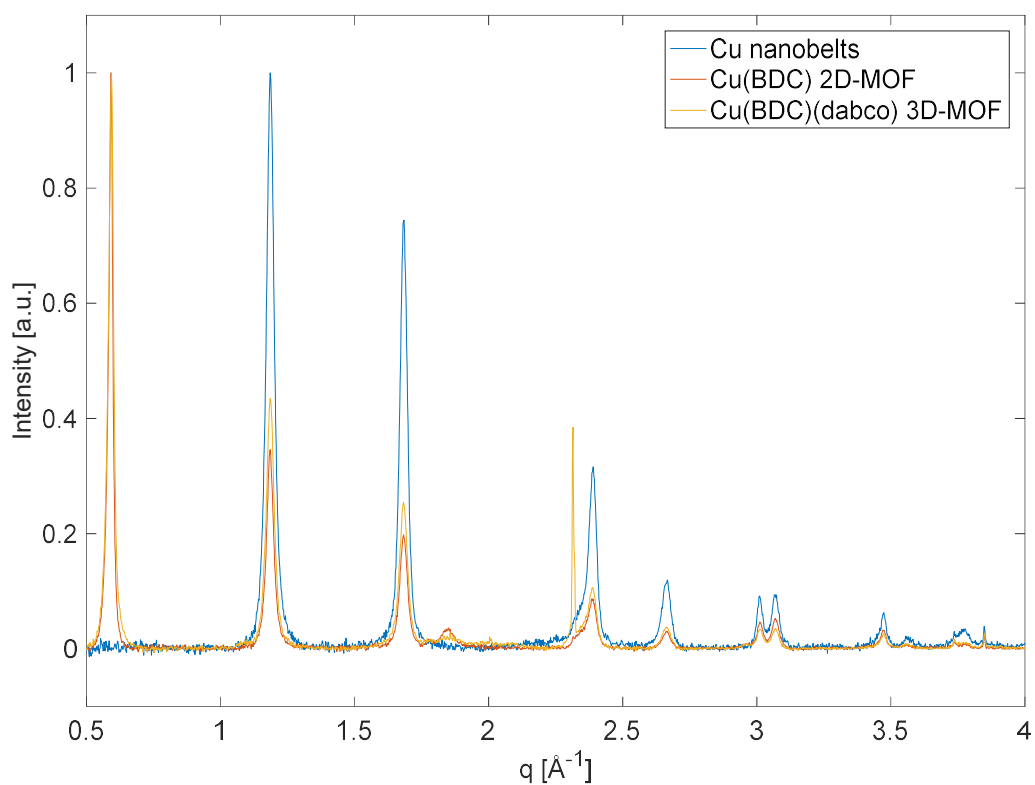
Figure 32 XRD patterns of oriented copper hydroxide nanobelts, 2-dimensional Cu(BDC)-MOF and 3-dimensional Cu(BDC)(dabco)- MOF

One can see, that both MOFs show the same structural features in specular direction. This is not surprising, as the linker in the out-of-plane direction for both MOFs is the same, and they differ only by in-plane linkage and ordering.

It is apparent that specular XRD does not offer sufficient information to understand the epitaxial relationship for the MOFs in question, although showing the uniaxial alignment for the nanobelt substrate quite nicely. Furthermore, the matching of the substrate and the MOFs peaks hint towards their epitaxial relationship. To gain further understanding on the ordering of the material, as a next step X-ray pole figures are measured.

6. Pole figures

The pole figure analysis is split up into a chapter for the plain copper nanobelt substrate and one for the MOFs on top of the nanobelts.

6.1. Copper nanobelt substrate pole figures

As a first step, pole figures on the copper nanobelt substrate are measured. Figure 33 shows the resulting pole figures on 5 different peaks. The data was gathered with a step size of 2° in both ψ and ϕ and a time per step of 1.5 s, resulting in a measurement time of 3.5 hours each. The data treatment is done with the Software tool *Stereopole* [51].
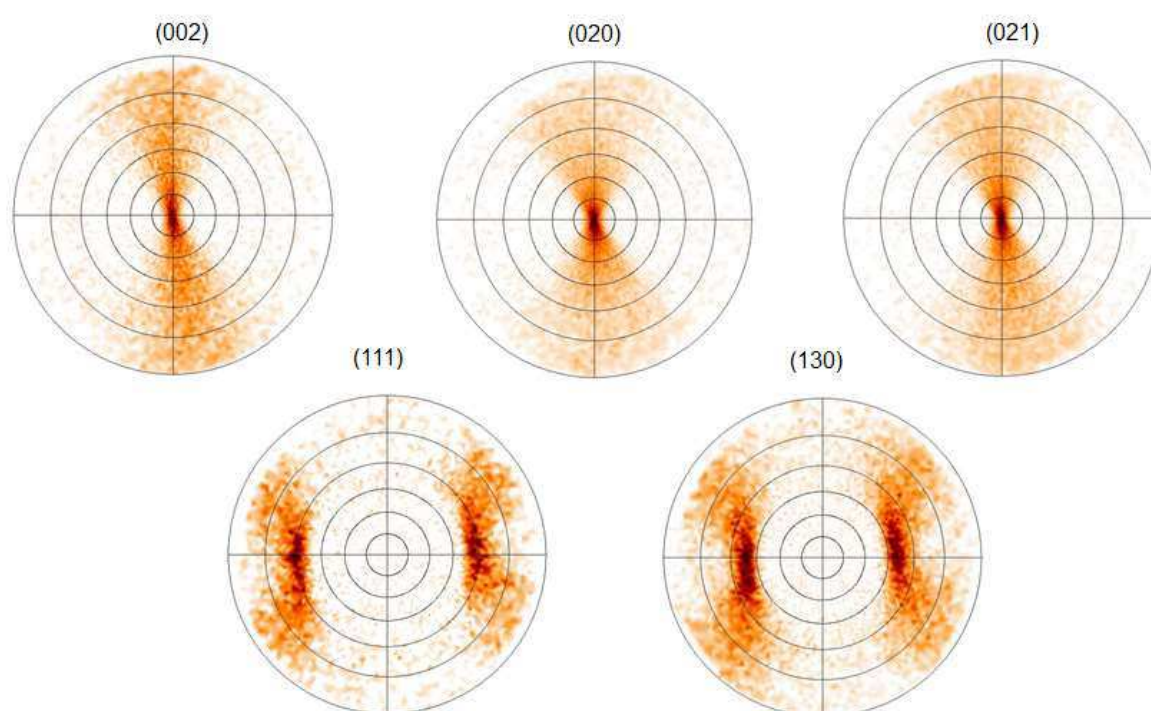

Figure 33 Pole figures, measured on oriented copper nanobelt substrate. The peak, the pole figure is measured on, is indicated above.

For all the out-of-plane peaks (h=0) the measured signal corresponds to the expected shape of an uniaxially aligned sample, which, in the ideal case would look like a straight line. The spreading of the intensity at larger tilt angles can be attributed to defocussing of the x-ray beam. The same goes for the pole figures on the in-plane peaks (h≠0). An ideal pole figure of a uniaxial oriented sample in in-plane direction would have two spots at a certain ψ-value, 180° in ϕ apart. Figure 34 qualitatively shows the expected pole figure for ideal uniaxial samples.
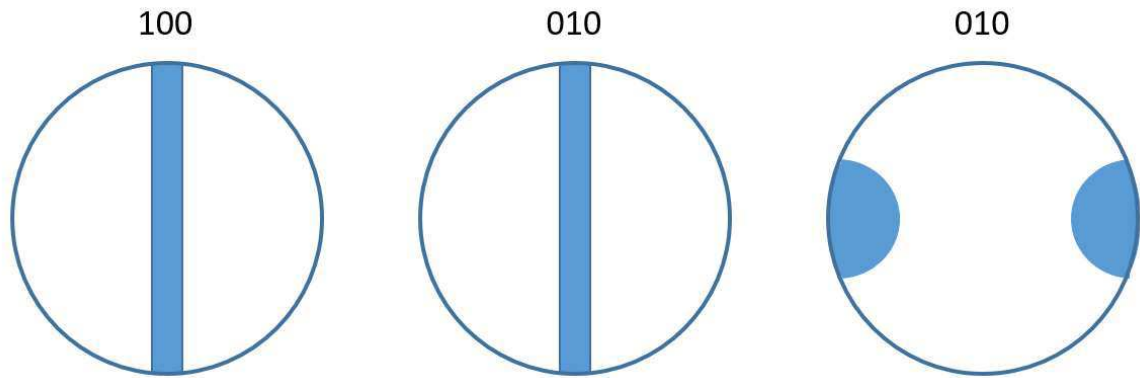
Figure 34 Representative pole figure for uniaxial alignment.

To further understand the in-plane ordering a repeated measurement on the 111 peak is performed. The step sizes in ψ and ϕ are set to 3° and 4° respectively and the time per step is set to 10 s, resulting in a total measurement time of about 8 hours. To study the contributions of different crystal orientations on the measured intensity, one uses *Stereopole,* to calculate the location of individual reflexes for different crystallite orientations. If the calculated intensity location fit the measured data, one can thus deduce the orientation of individual crystallites, which contribute to the signal. Figure 35 shows the measured pole figure and calculated positions for the signal coming from crystallites oriented in [001], [010], [011], [023] and [053] direction.
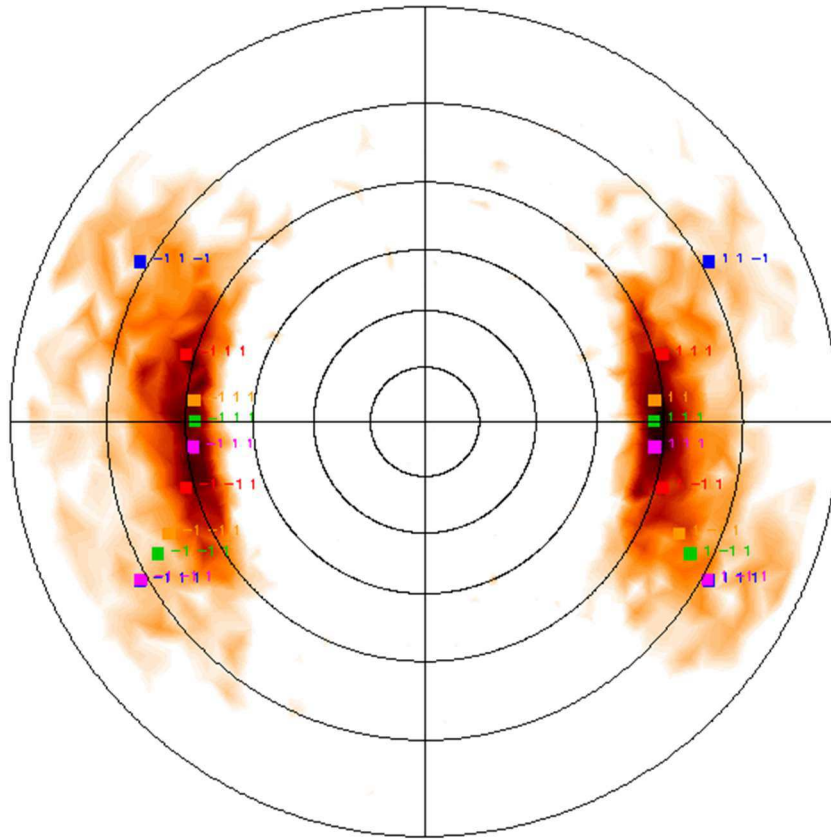
Figure 35 Pole figure on the (111) peak of oriented copper nanobelt substrate, with calculated peak positions for several crystallites in-plane of the sample.

From the matching of calculated peak positions with the measured intensity, one can see that not only crystals, with single crystallographic direction contribute to the signal, but in fact the whole family of crystallites, oriented in [0kl] direction, are present on the sample. The nanobelt substrate is thus only oriented fully in [100] direction. With this information, combined with the intensity spread at higher tilt angles in the out-of-plane pole figures a model for the orientation of the nanobelts can be moulded. In Figure 36 a rendering of the ideally expected nanobelt alignment on the wafer, as well as the real, slightly disordered, alignment of the copper nanobelts is visible.
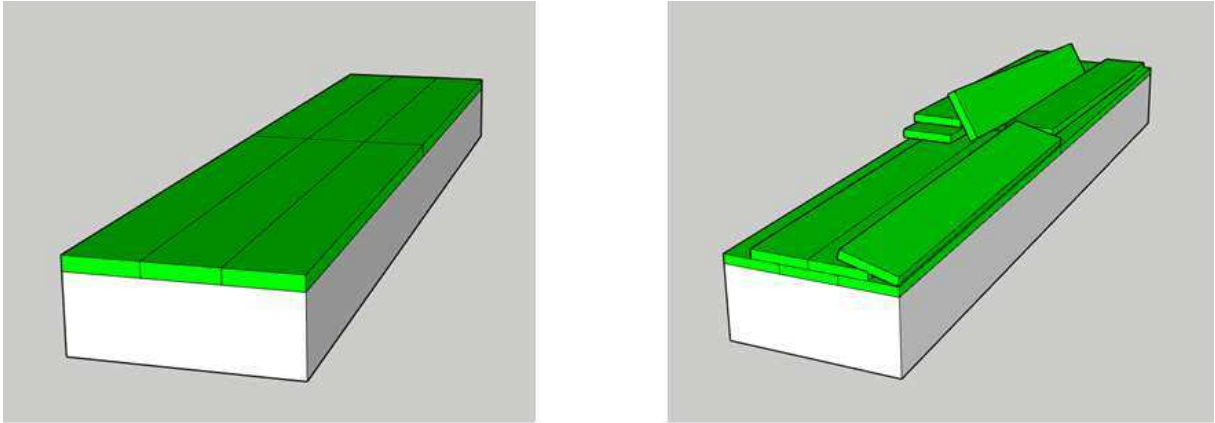
Figure 36 Left: Ideal flat-lying copper nanobelts, oriented in one direction. Right: Real copper nanobelt orientation, showing mismatches, although still conserving the general orientation in one direction.

It is so far apparent, that the orientation of the nanobelt substrate is not perfect, but the preferential orientation in one direction can be confirmed.

6.2. MOF pole figures

As a next step, a pole figure on the out-of-plane peak of the 2-dimensional Cu(BDC) MOF is measured. The step sizes in ψ and ϕ are set to 2° and 4° respectively and the time per step is set to 15 s, resulting in a total measurement time of about 17 hours. Figure 37 shows the resulting pole figure.
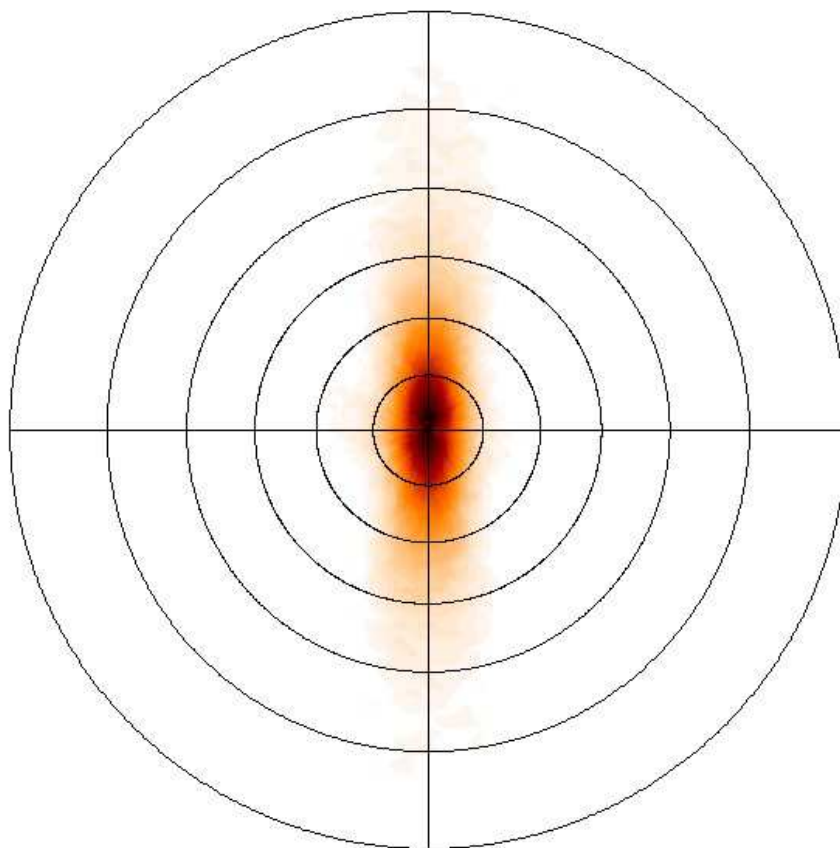
Figure 37 Pole figure on the (100) peak at q= 0.5881 Å^{-1} of 2-dimensional Cu(BDC) MOF, grown on oriented copper nanobelt substrate.

The same uniaxial features, as for the oriented nanobelt substrate are visible, with even less spread in intensity at higher ψ-values. The MOF does in-fact grow with the same overall alignment, as the underlying nanobelt substrate. Because the intensity is more sharply peaked in the middle, it can be assumed, that, although the nanobelt substrate may show some misalignment, the MOFs still preferentially grow on those nanobelts, which are oriented properly. Because there is only one peak in the spectrum, that is independent of the nanobelt substrate, further pole figures would mostly show signal, coming from the substrate and therefore another technique, which is able to access in-plane peaks is necessary.

7. Grazing Incidence X-ray Diffraction (GIXD)

As for the pole figure measurement, the GIXD analysis is split into first investigating the plain copper hydroxide substrate and then the MOFs, grown on top of the substrate.

7.1. GIXD on copper nanobelt substrate

GIXD measurements were done at the Elettra Synchrotron in Trieste. For a first characterization, as with the other measurement methods, the plain nanobelt substrate gets measured. The alignment is done in two steps. The first step consists of shining a laser onto the sample and recording the position of the reflected laser spot during rotation of the sample. In a perfectly flat aligned sample, the position of the reflected beam should remain constant, whereas in a misaligned sample the reflected beam, would follow an ellipses path. Changing the orientation of the sample by precise screws on the sample tray, therefore allows to align the sample to be lying flat, with respect to the incident beam. The second step of alignment is for the height of the sample with respect to the incident beam. For this the sample is moved along the z-axis, with a fixed incident angle of the X-ray beam and the resulting signal is measured. The z-position where the first and where the last diffraction signal appears indicate the upper and lower sample edge. The mean of those two height values should be in the middle of the sample. This whole procedure is necessary to allow, that the X-ray beam hits the sample directly in the middle and at a well-defined angle. The measurement of the GIXD-map is done after successful alignment. The measurement time for all the samples is set to 1 s, because longer measurement times would result in exceeding the 1 million counts limit of the used detector. For the oriented copper nanobelt sample, measurements are done while rotating the sample in 2° steps, resulting in a total of 180 individual measurements after a full rotation. All the data treatment and visualization after the measurement is done in the software *GIDVis* [40]. In Figure 38 the GIXD-Map for the oriented copper nanobelt substrate is shown. For full angular information, the 180 individual images are summed together, thereby also improving signal to noise ratio.
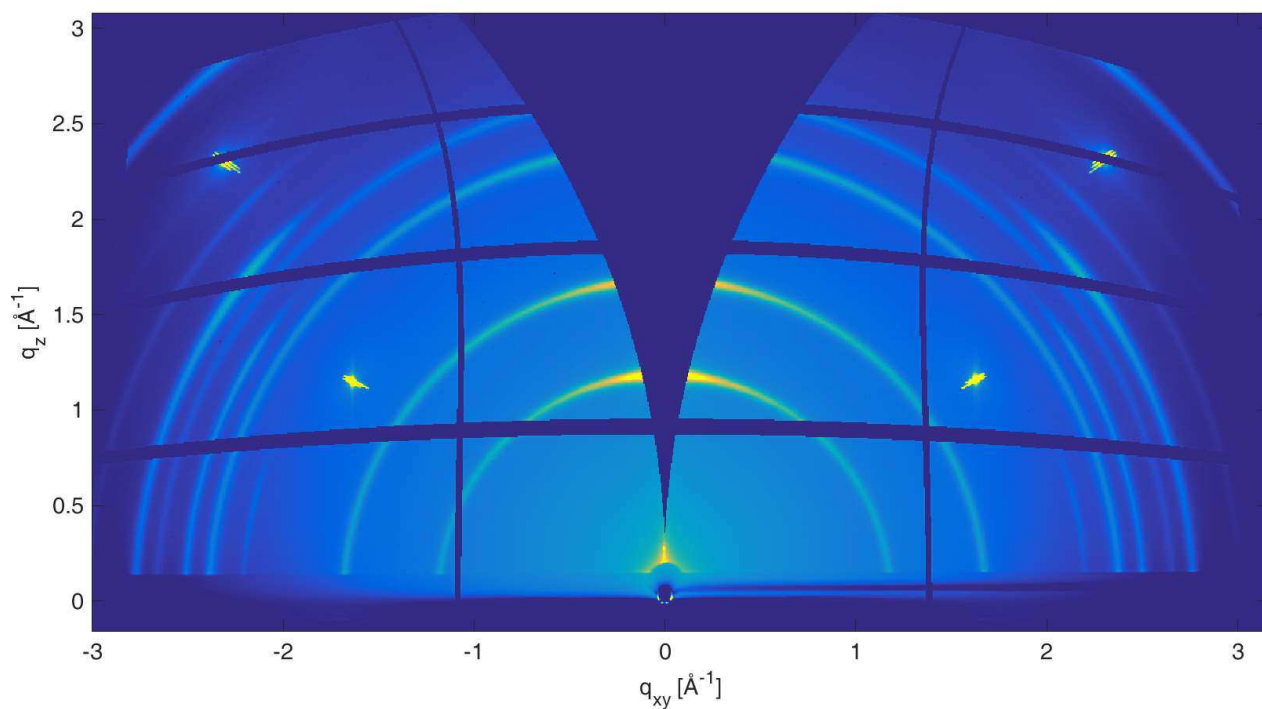
Figure 38 GIXD-Map of the oriented copper nanobelt substrate

One can see intensity at rings of constant |q|, now having the full information of both out-of-plane as well as in-plane diffraction. As the image is a result of summing images from a full 360 ° rotation, the features are similar in the left and right half of the image. Therefore, the analysis can be reduced to one half of the image above. To match the intensity in the GIXD-Map with the crystal structure of the material under question, the positions of the peaks can be calculated from the structural information in *GIDVis*. Furthermore, the structure factor can be calculated, indicating if certain peaks are forbidden due to symmetry. Figure 39 shows the right side of Figure 38 as well as the calculated peak positions and indices for copper hydroxide, lying on Debye-Scherrer rings. A circle is drawn around every peak, the area of which is proportional to the structure factor.
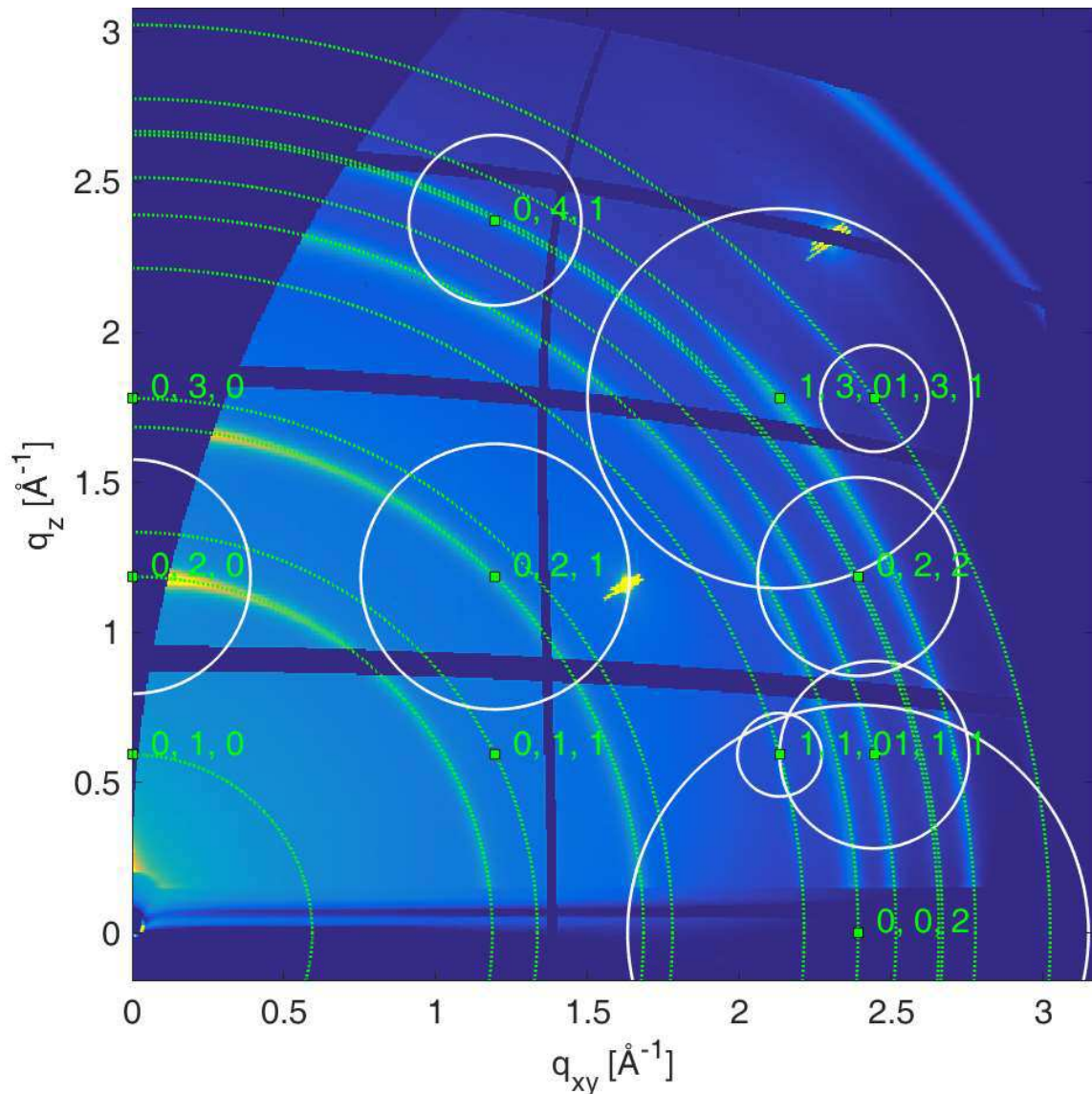
Figure 39 GIXD-Map of oriented copper nanobelts, with indexation for peak positions, rings of constant |q| and structure factor

One can see that all the peaks can be indexed successfully, showing the usage of *GIDVis* to index GIXD-maps of a material with a known crystal structure. The two single bright spots, can be identified as coming from the silicon substrate, on which the nanobelts are lying upon.

7.2. GIXD on MOF samples

In a next step a sample with 2-dimensional MOFS, grown on top of oriented copper nanobelts gets measured in the synchrotron. The alignment procedure is the same as above, but turned out to be slightly more difficult, as the optical reflectivity of the MOF-covered sample is lower, making the orientation-alignment by usage of a reflected laser beam more prone to errors. Like the plain nanobelt substrate, a measurement time of 1 s

each is chosen, and 180 images during a full rotation are taken. Figure 40 shows the right half of the integrated signal from all the 180 images.
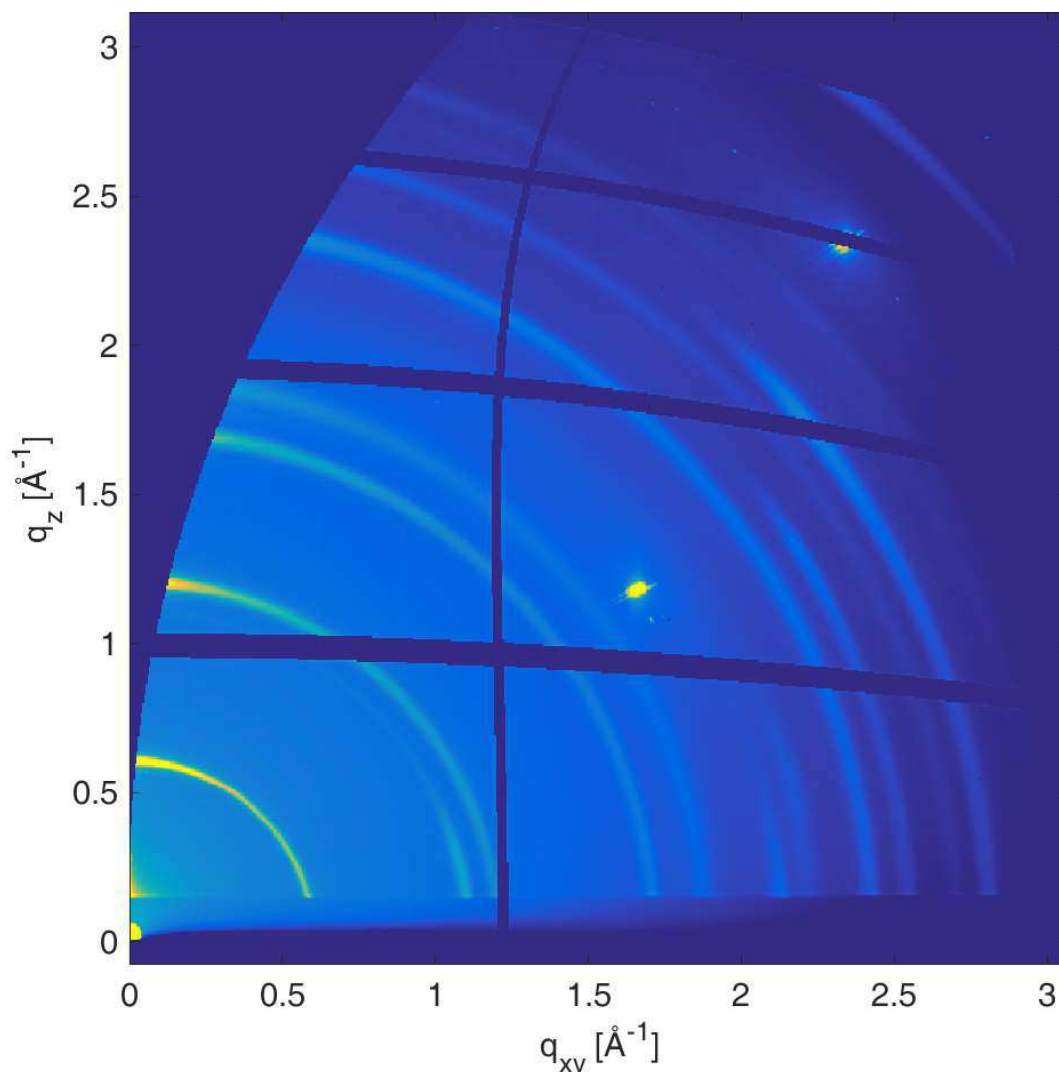

Figure 40 GIXD-Map of 2-dimensional Cu(BDC)-MOF, grown epitaxial on oriented copper nanobelt substrate.

Apart from the one out-of-plane peak at $|q|=0.58$ Å^{-1}, an additional in-plane peak at about $|q|=1.1$ Å^{-1} is visible. A complete structure solution, based on two peaks alone, is a futile effort, so instead a different approach is taken. Starting from the structure of the Cu(BDC)-MOF-Form 2, from Figure 30, which has a solved crystal structure, that fits decently to the epitaxial grown Cu(BDC)-MOF, the unit cell axes are tweaked until the calculated peak positions fit the measured ones at $|q|=0.58$ Å^{-1} and $|q|=1.1$ Å^{-1}. Furthermore, no additional peaks should be introduced, that are not located at the same position as the peaks from the oriented nanobelt substrate. The resulting indexing is shown in Figure 41.
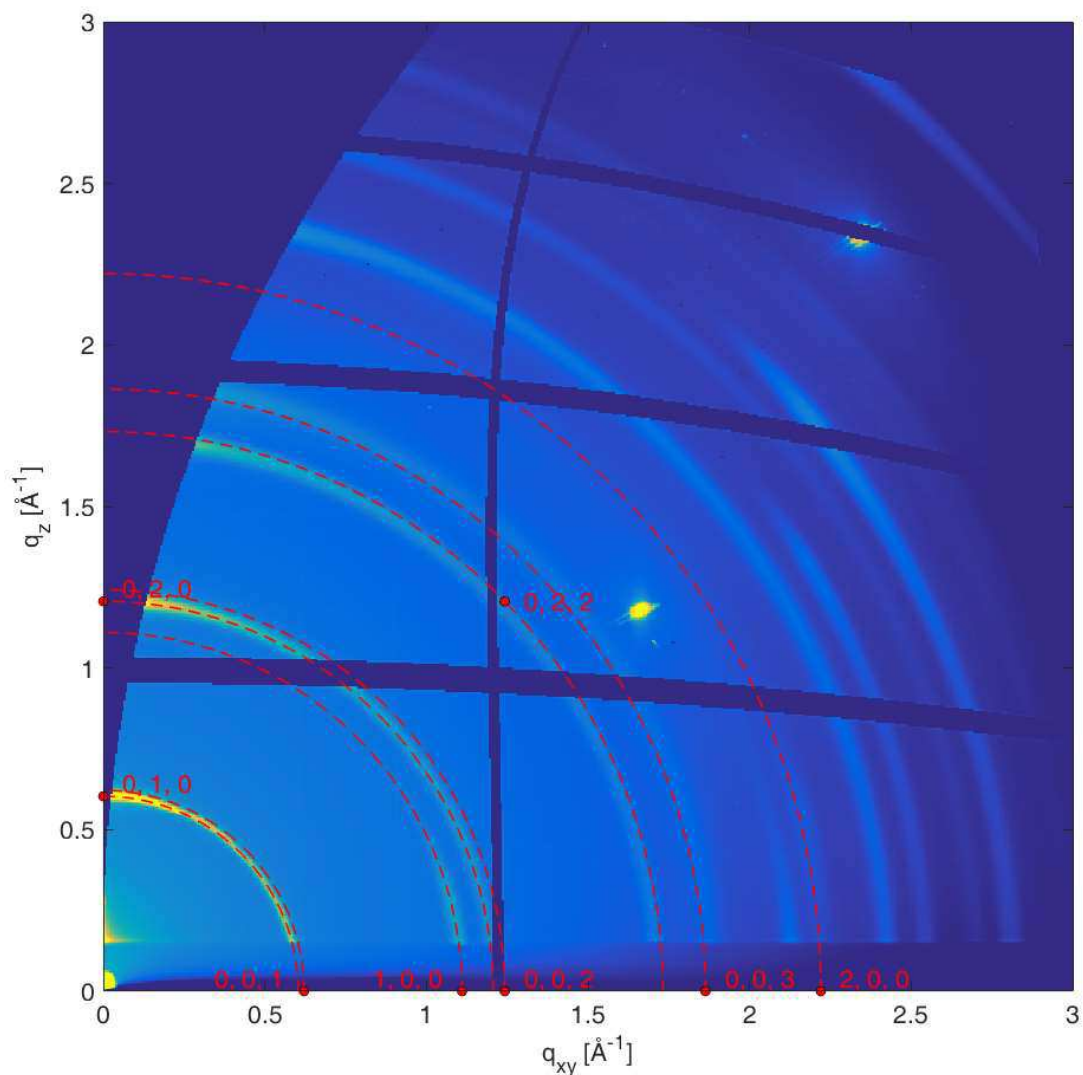
Figure 41 GIXD- Map of Cu(BDC)-MOF on oriented copper nanobelt substrate, with attempt at indexation, based on Cu(BDC) Form 2.

With the indexation above, the unit cell lengths can be determined and are summarized in Table 1, together with the proposed lengths from Falcaro et al. [2] and the unit cell lengths for the bulk Cu(BDC)-MOF phase [49].

Table 1 Summary of unit cell parameters for the Cu(BDC)-MOF, reported as an ideal structure, as measured and as solved for the bulk phase.

	a [Å]	b [Å]	c [Å]
Reported	5.8	10.6	10.6
Measured	5.659	10.615	10.115
Bulk Structure	5.2502	10.768	9.6690

It is apparent, that there is discrepancy between the reported structure, with unit cell axis b=c, and the measured one. The unit cell axis for the Cu(BDC)-MOF corresponds to the length of the BDC linker, which appears to show anisotropy, depending on, if it points in the out-of-plane or in the in-plane direction. This anisotropy is also present in the bulk phase. Further study should be undertaken to understand the exact structure of the epitaxially grown Cu(BDC)-MOF on copper nanobelts but a preliminary model can be constructed. Figure 42 shows a model of a 2-dimensional MOF sheet, standing on copper nanobelt substrate, with indication of linker lengths.
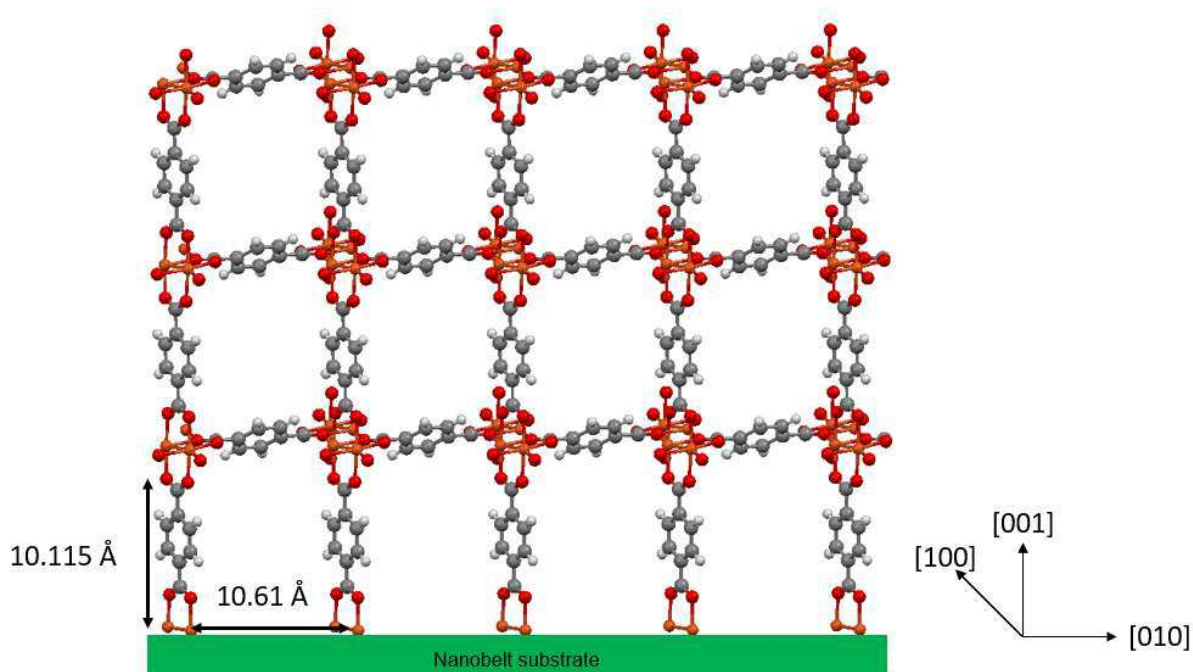
Figure 42 Structural model of 2-dimensional MOF sheet.

Moreover, the GIXD-Maps can be used to gather further information on the epitaxial relationship between substrate and MOF. Because the sample is rotated during measurement, the angular dependence of the signal can be plotted. Figure 43 shows the angular dependence of the intensity on the MOF peaks at $|q|=0.58$ Å^{-1} in in-plane direction and a comparison with the angular dependence for the signal of the nanobelt substrate peak at $|q|=1.186$ Å^{-1}.
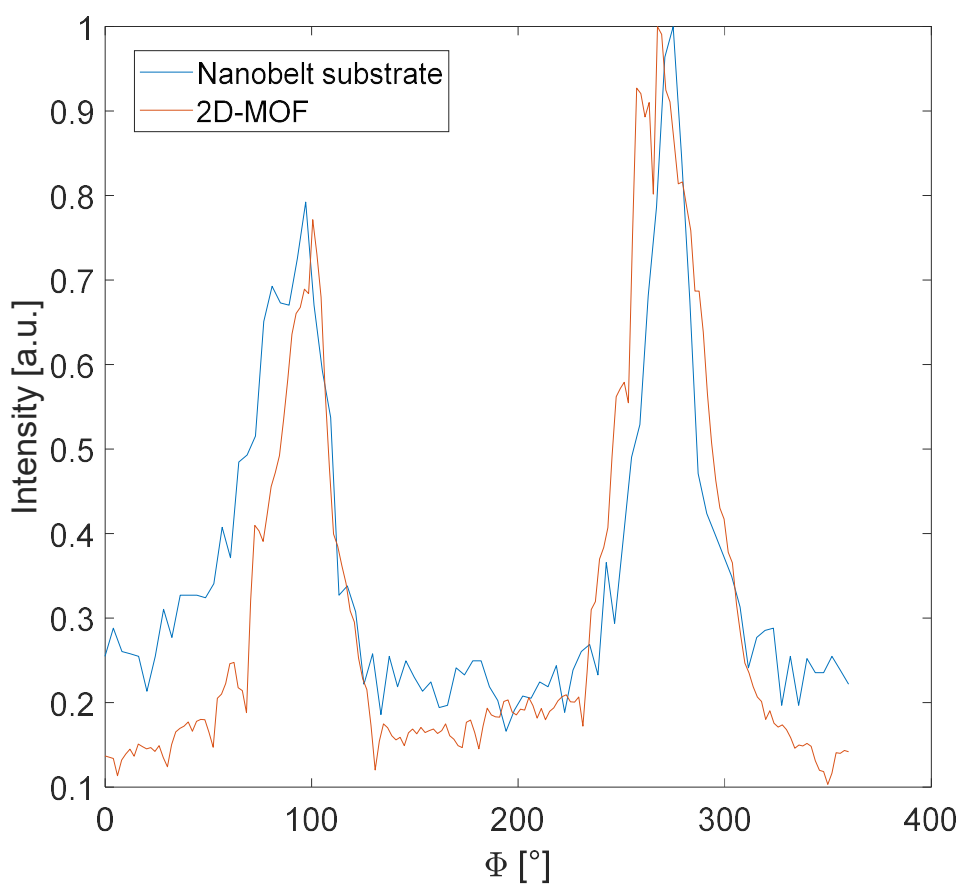
Figure 43 Angular dependence of the diffraction signal from the nanobelt substrate peak and from the 2-dimensional MOF peak.

It is apparent that a similar angular relation is present in both substrate and MOF.

In a next step a GIXD-Map of the 3-dimensional Cu(BDC)(dabco)-MOF is measured. The same measurement parameters as before are used and the sample is rotated during measurement. The integrated signal from a full rotation is shown in Figure 44.
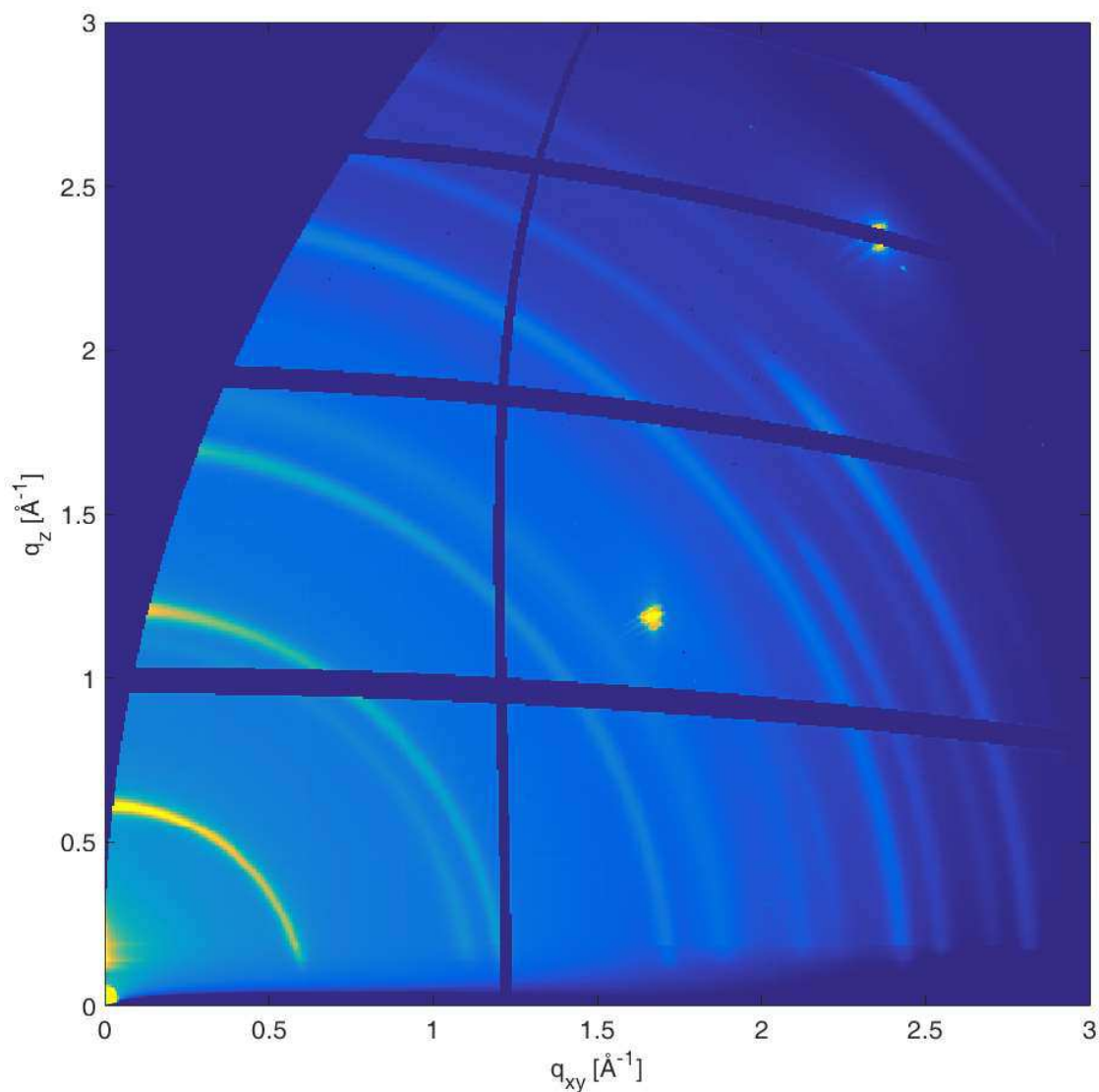
Figure 44 GIXD-Map of 3-dimensional Cu(BDC)(dabco)-MOF

Surprisingly, the measurement, shows the exact same signal as for the 2-dimensional MOF. To understand this and to eliminate the possibility that the preparation recipe only yields 2-dimensional Cu(BDC)-MOF instead of Cu(BDC)(dabco)-MOF, a powder sample is prepared for both MOFs. The recipe for the powders is described in Chapter 3. After preparation the powders are measured in-house and the signal is compared to the GIXD signal, integrated over rings of constant |q|. Figure 45 shows the comparison between freshly prepared MOF powders and integrated scans from GIXD data.
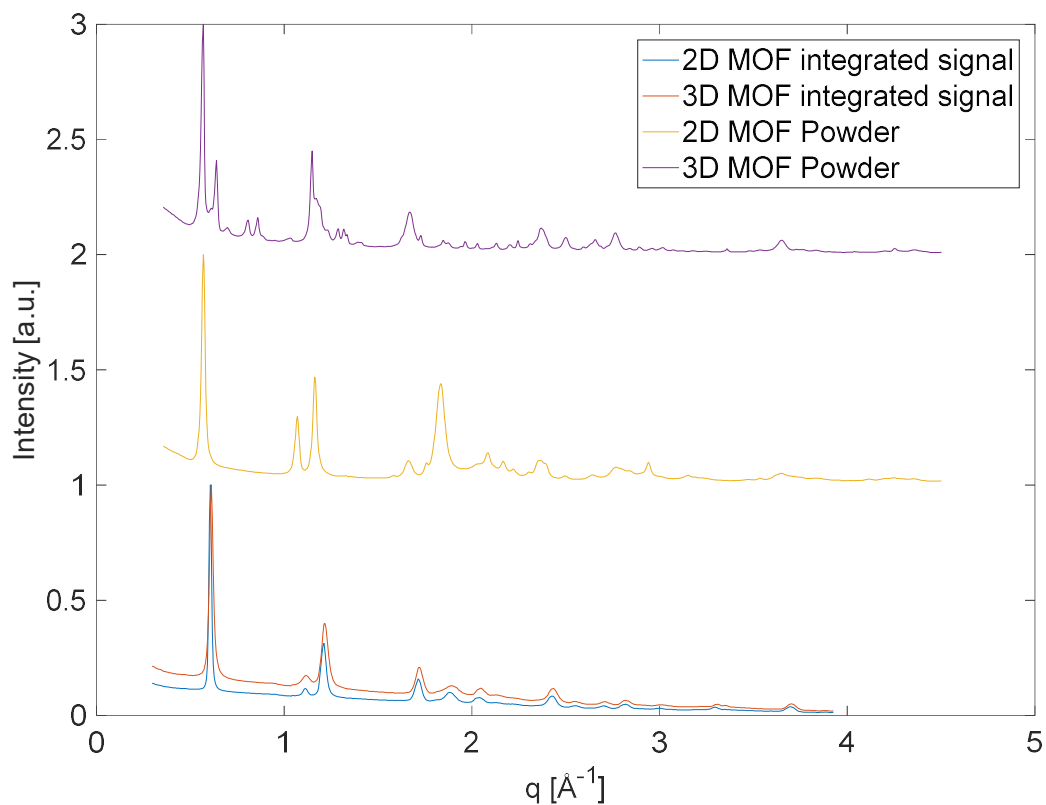
Figure 45 Comparison between freshly synthesised MOF powders and those, measured in GIXD.

It is apparent, that the powders show certainly different structural features, whereas the integrated signal from the GIXD image is very similar. The preparation recipes do in-fact yield different MOFs, but the 3-dimensional Cu(BDC)(dabco)-MOF appears not to be stable enough, to be measured weeks after synthesis. A structural characterization of the 3-dimensional MOF is therefore not possible, but it can be noted that the Cu(BDC)(dabco)-MOF converts to Cu(BDC)-MOF. If this conversion happens spontaneous or was induced by repeated X-ray bombardment is unclear, for the time being.

8. GIXDPF

With the method, described in section 2.5., it is now possible to calculate pole figures out of GIXD-maps. To check if the method works, the GIXD-Maps for the plain copper nanobelt substrate is measured and pole figures are calculated on several peaks. Afterwards they are compared to in-house measured pole figures on the same peaks. The results of the comparison are presented in Figure 46.
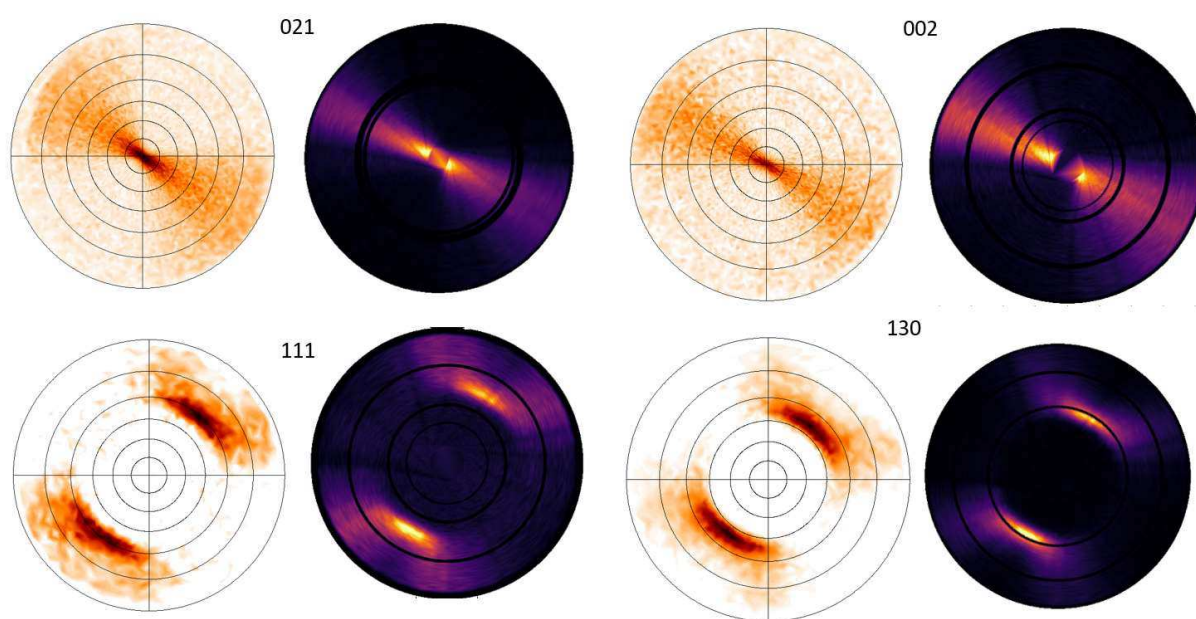
Figure 46 Comparison between measured (left) and calculated (right) pole figures on oriented copper nanobelt substrate.

It is visible, that the method is indeed able to reproduce the features, that were measured in-house very accurately. Now one can calculate pole figures on the two MOF peaks, and compare them to the pole figure of the underlying substrate, to confirm the aligned growth. Figure 47 shows calculated pole figures from the MOF in-plane and out-of-plane peak and a comparison with the signal from the nanobelt substrate.
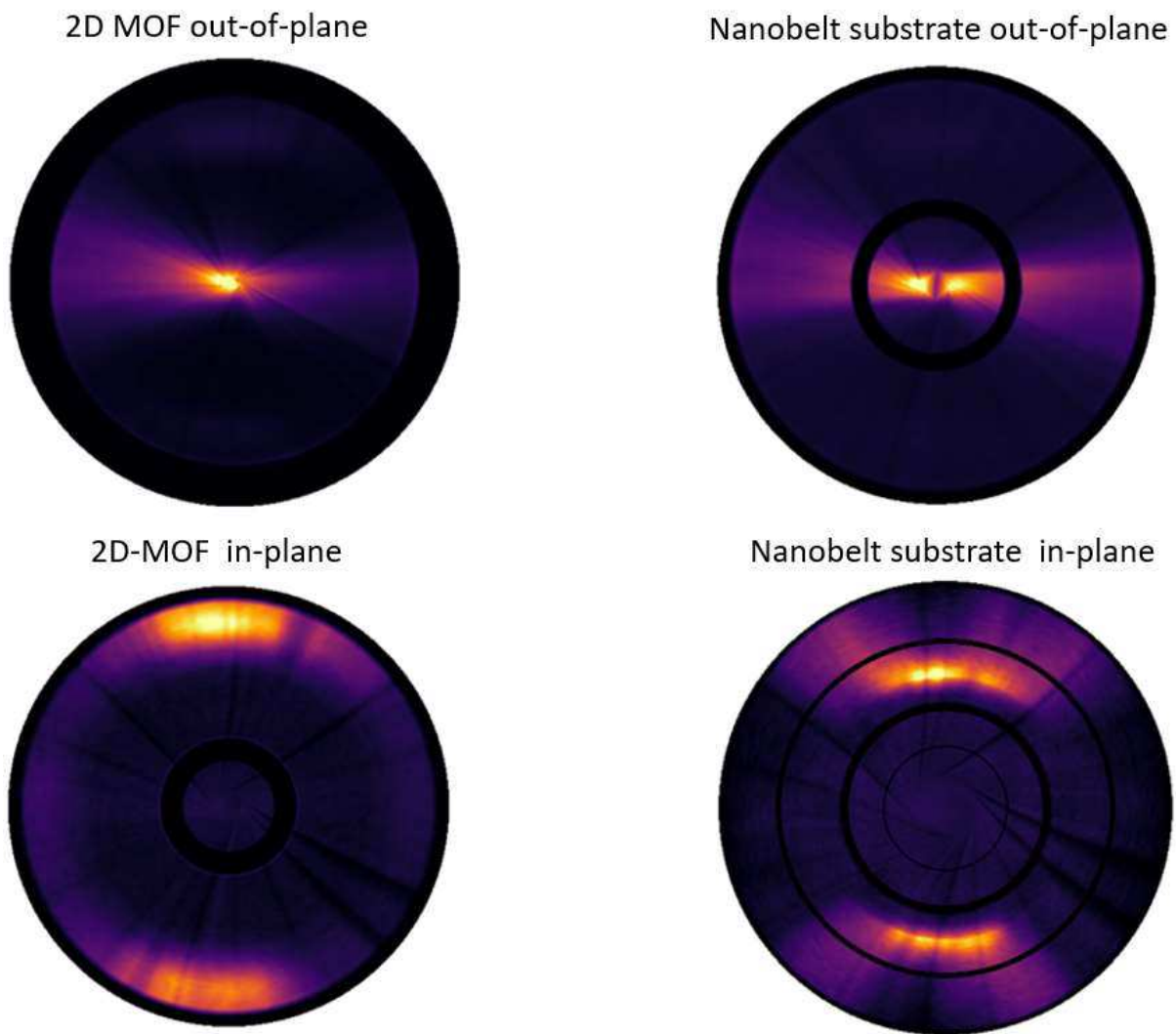
Figure 47 Comparison of pole figures, calculated from 2-dimensional MOF and from oriented nanobelt substrate.

With this measurement the epitaxial ordering can be summarized as (001) MOF || (010) of copper hydroxide and (100) MOF || (100) of copper hydroxide.

The newly developed method of GIXDPF proves to be an efficient method of gaining pole figure information, even if the peaks are not accessible with conventional methods.

In a last step, the samples, which were prepared as 3-dimensional Cu(BDC)(dabco) MOF, but turned out to have been degraded back to Cu(BDC) MOF, were checked for their orientational alignment via GIXDPF. Figure 48 shows the result of the GIXDPF calculation on the out-of-plane peak as well as on the in-plane peak of the deteriorated 3-dimensional MOF.
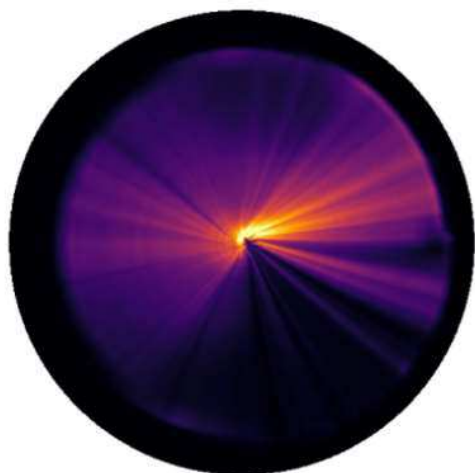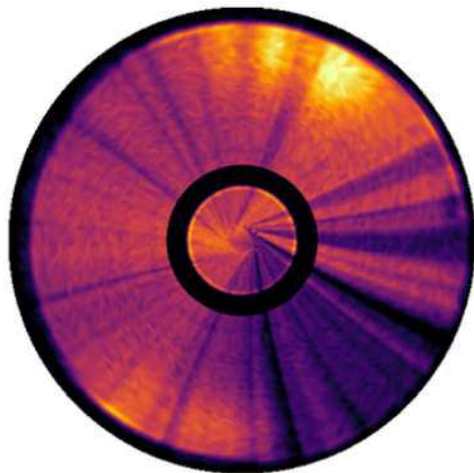
Figure 48 Calculated pole figure on the peaks of the Cu(BDC)(dabco) sample, which did degrade to Cu(BDC) MOF.

Some aligned features are visible, but it appears that the 3-dimensional MOF Cu(BDC)(dabco) is not stable for long times, also destroying most of the alignment when degrading.

9. Ligand Exchange reaction

Ligand Exchange reaction serve as a powerful tool, when dealing with MOFs, because it allows to change the MOFs properties after synthesis. For this a model ligand exchange reaction is studied in this thesis.

To study the effect of the functionalisation of the grown MOF, the ligand exchange reaction is done, with the method described in Chapter 4.4. The starting material for the conversion is a freshly prepared 2-dimensional Cu(BDC)-MOF on oriented copper nanobelt substrate. After each reaction cycle, the sample is measured with XRD. The resulting spectra are visible in Figure 49.
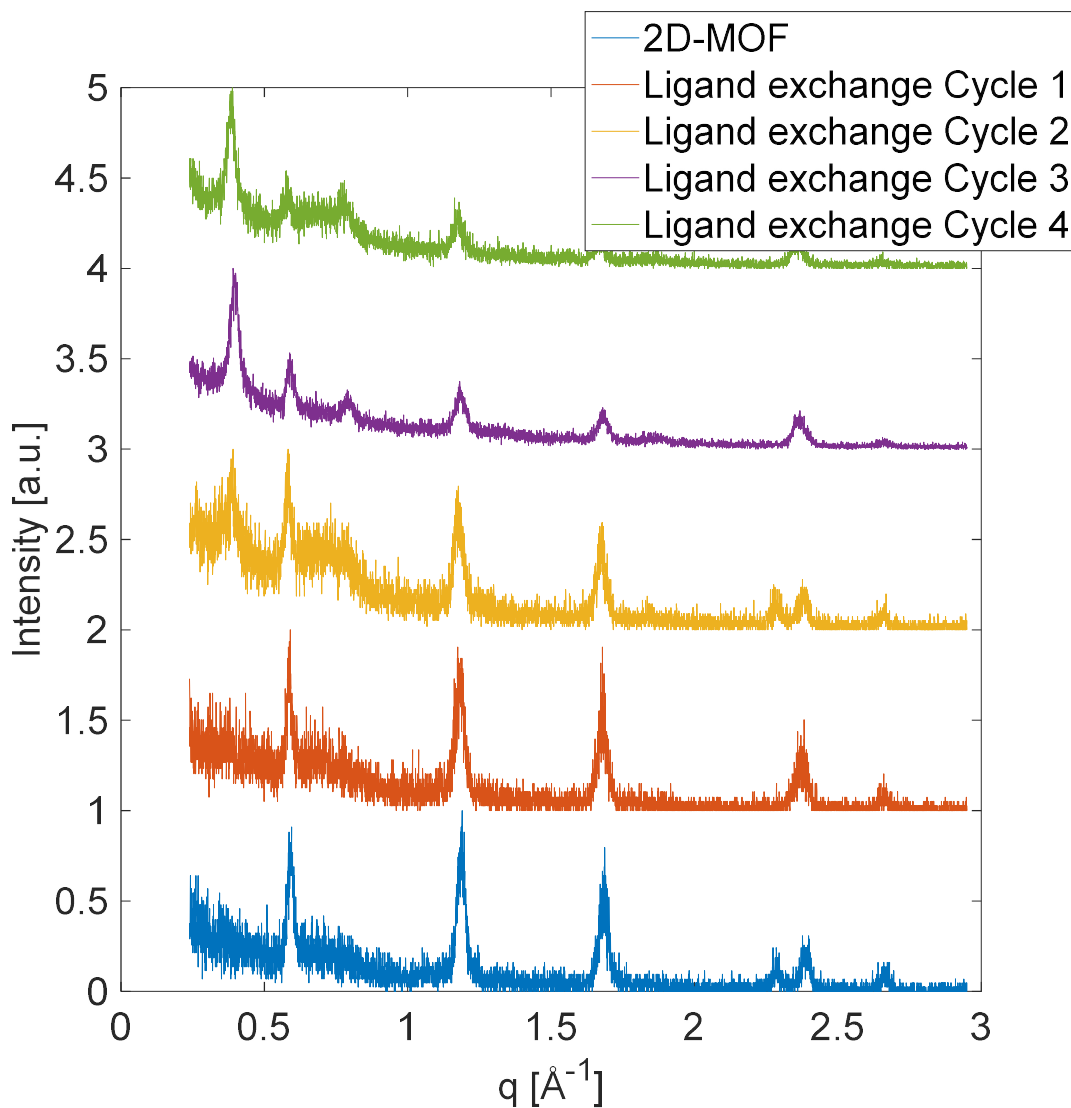
Figure 49 XRD patterns of 2-dimensional Cu(BDC)-MOF before and after each cycle of the ligand exchange reaction.

A very significant structural change is visible, indicated by the decline of the out-of-plane linker peak at q=0.590 Å^{-1} and the appearance of a new peak at q=0.384 Å^{-1}. Further reaction cycles, did not yield any change of signal, as was previously confirmed by FTIR. It is apparent, that in the case of trying to functionalise the BDC linker with an amino group, the exchange reaction is not done independent of the structure.

Because the specular XRD measurement showed a very significant structural change, the sample after the 5th ligand exchange cycle was measured in GIXD to access in-plane information and to try index the peaks. Figure 50 shows the GIXD-Map for the 2-dimensional Cu(BDC)-MOF on oriented nanobelt substrate after 5 ligand exchange cycles.
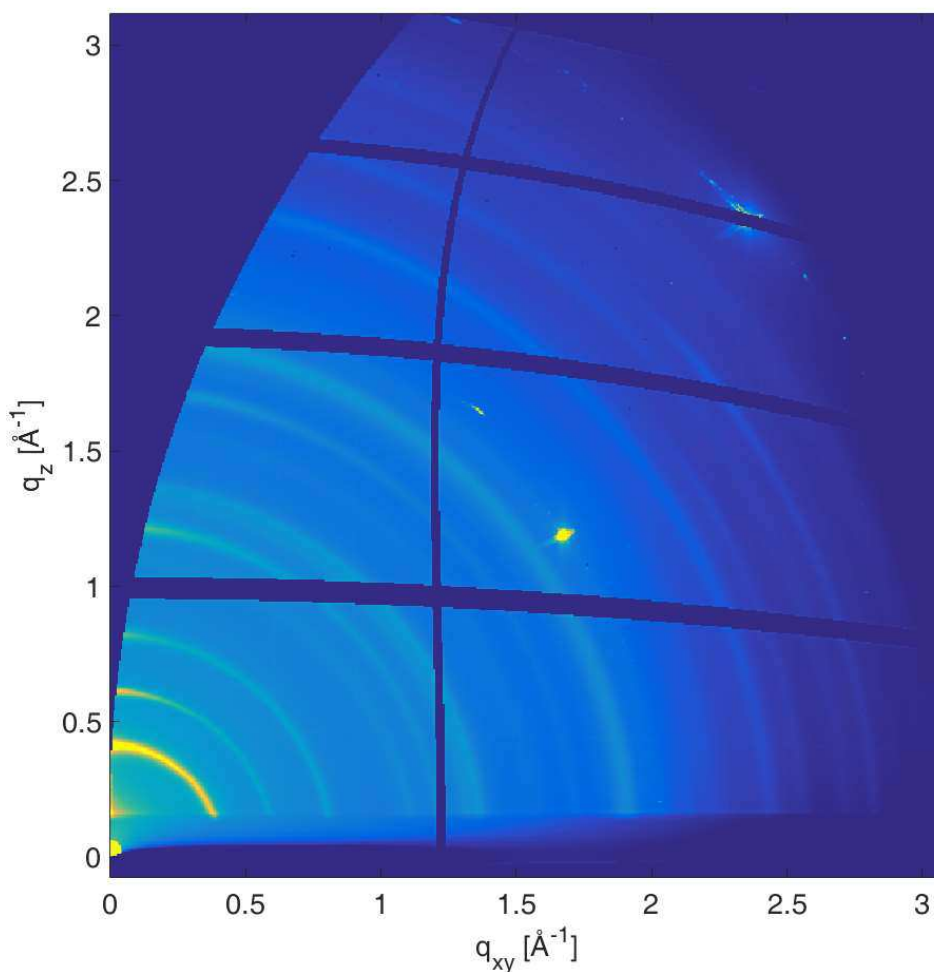
Figure 50 GIXD-Map of Cu(BDC) after 5 ligand exchange cycles.

An approach to index the rings is undertaken, starting from the structure of the 2-dimensional MOF sheet, with a=5.659 Å, b= 10.615 Å and c= 10.115 Å. The unit cell parameters are changed until the calculated signal fits nicely to the measured one, with all measured peaks either indexed with the MOF or the nanobelt substrate. The areas where

the rings are more smeared out at q=1.35 Å^{-1} and at q=1.92 Å^{-1} could be indexed with unreacted NH$_2$-BDC-linker material. Figure 51 shows the result of the indexing.
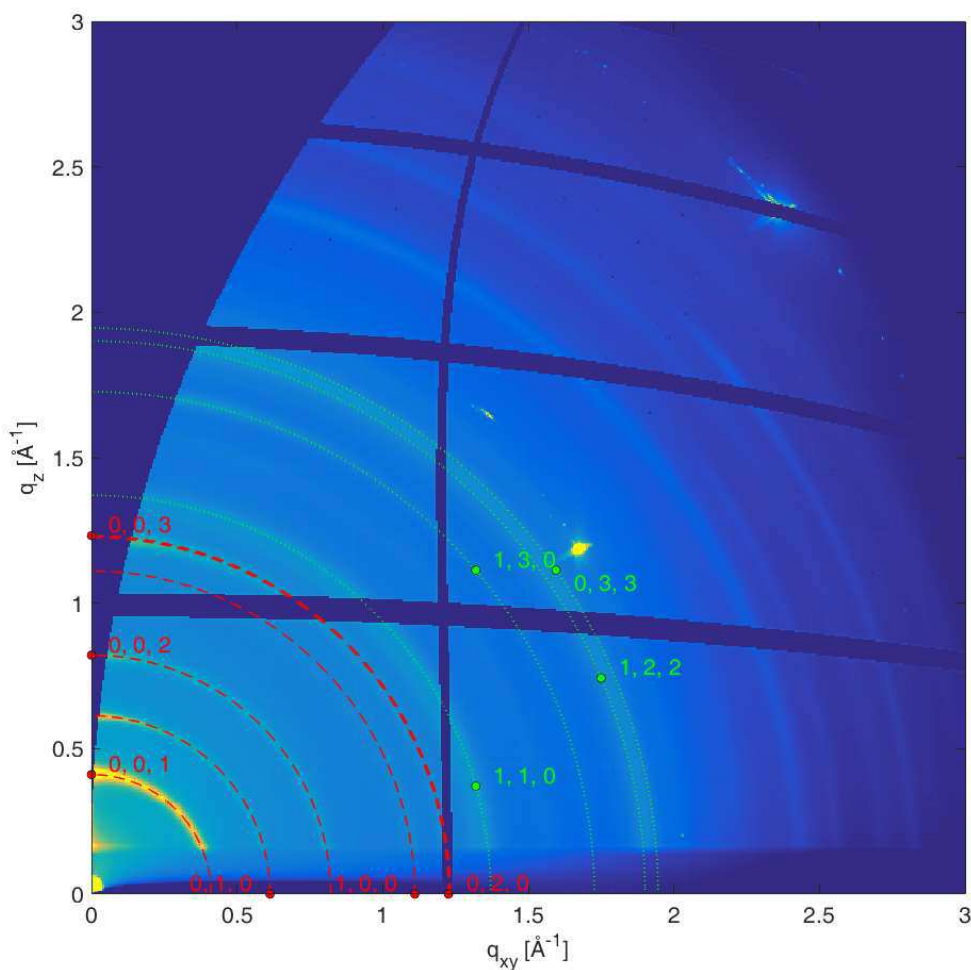
Figure 51 GIXD-Map of Cu(BDC) after 5 ligand exchange cycles, with indexation. Red colour indicates the MOF material and green colour the unreacted NH$_2$-BDC-linker material.

The unit cell lengths before and after the conversion are summarized in Table 2.

Table 2 Unit cell lengths of MOF material before and after ligand exchange reaction

	a [Å]	b [Å]	c [Å]
Before ligand exchange	5.659	10.615	10.115
After ligand exchange	5.659	10.250	15.300

A very significant anisotropic elongation along the c-axis (the out-of-plane axis) is visible. Further work must be done, to understand the ligand exchange process in the case of Cu(BDC)-> Cu(BDC-NH$_2$), but it can be noted, that amino-functionalisation cannot be done independent of the crystal structure in the present case.

10. Error Estimation and Discussion

This chapter is dedicated to give an estimate on the boundaries of the methods used in this thesis.

The biggest factor on the uncertainty of the results presented is the absence of many individual peaks from the MOF, to do the analysis. This is apparent in this case, because due to epitaxy the substrates and the MOFs peaks will always lie on top of each other. Independent analysis on the MOF alone is therefore not possible, except for the first peaks. A full structural solution based on many independent X-ray peaks, as is normally done is therefore not applicable. The alternative is to start from a given crystal structure and tweak the unit cell axes to fit the measurement. This can be done very precisely, as the position of the diffraction rings is measured to a high degree of accuracy in GIXD, but one must assume a certain degree of similarity between the MOFs, grown on top of a nanobelt substrate, and the deposited crystal structure for the MOF, which is in powder form, without an epitaxial relationship with the substrate. A change in the crystal system of the epitaxially grown MOF would therefore not be possible to measure, but given the crystal symmetry is conserved, the lattice spacings are determined to a high degree of accuracy. Another problematic factor is currently the difficulty in producing nicely oriented substrates and the lack of large amounts of samples because of this. If the method of fabricating good substrates could be improved, more samples could have been prepared and the influence of e.g. MOF thickness on the diffraction signal could be evaluated. This would show, if the MOFs structure is different in very thin samples, compared to very thick samples, indicating a more surface-induced phase that gradually becomes more bulk-like when growing. To study this the methodology of preparing nicely oriented samples was tried to be improved, but no alternative method could yield better substrates, then doing the nanobelt transfer very slowly by hand.

Furthermore, the indexation of MOFs, in general, is difficult as the diversity and novelty of MOFs presents many structures that have yet to be solved. In the case of an epitaxial grown MOF on top of a nanobelt substrate, this is even more severe, as this idea has not been utilised before.

Considering the estimation of the orientational alignment by X-ray pole figures and subsequently by GIXDPF, the uniaxial alignment of the substrate was shown. When comparing pole figures from the MOF with pole figures from the substrate, the orientational matching, indicates very directly that the idea to give a preferred orientation

to the MOF by using an aligned substrate is quite promising. Furthermore, it is shows that in epitaxial systems, the X-ray pole figure technique is very powerful to compare the crystals alignment with each other.

The newly developed method of GIXDPF, i.e. calculating pole figures from rotated GIXD, could be tested and yields results, that are in close agreement with conventional X-ray pole figure measurement. The big advantage, compared to conventional measurement is the fact that the whole reciprocal space is accessible in greatly reduced time. A measurement at the synchrotron to get the needed GIXD data is generally done in several minutes, whereas mapping all of reciprocal space via conventional pole figure method, could also be done, but would take several weeks of continuous measurement. In the case of peaks, lying very close to each other the method of GIXDPF also shows improvement to conventional pole figure measurement, as a precisely defined section of q-space can be analysed, opposed to an ever-present uncertainty in q, due to the spread of the X-ray beam in the experimental setup. GIXDPF is therefore a nice addition to the toolbox of data analysis when it comes to interpreting GIXD data.

The ligand exchange reaction could be studied, yielding unexpected results of a very anisotropic change in the unit cell lengths of the crystal. Indexation is again limited, due to the absence of many peaks, but the length of the out-of-plane linker alone is determined to a high degree of accuracy. A change in crystal system is again out of scope for the methods employed here. Further measurement on the ligand exchange reaction in the case of Cu(BDC) MOF, could yield insight, why the linker is only elongated in the out-of-plane direction.

11. Conclusion

The goal of this thesis was to use X-ray methods on a class of materials, prepared by a very novel approach. It should stand as a benchmark for using contemporary X-ray methods when dealing with an epitaxial grown MOF, yielding supplementary data for the analysis of this new material and helping to get insight in the crystallographic structure of MOFs, in general.

The oriented copper nanobelt substrate was measured via specular XRD, hinting towards the uniaxial order of the nanobelts, when comparing with powder diffraction data. X-ray pole figures ware measured, confirming the alignment, showing that there is still improvement on the method to align the individual nanobelts, which was used here.

The 2-dimensional MOF Cu(BDC) was studied via specular XRD, yielding very little information, as one is limited to information in the out-of-plane direction, where the peaks from substrate and from the MOF are not independent from each other, due to epitaxy. Using GIXD, one could acquire a measure for the unit cell parameters of this MOF, by comparing it to an already solved bulk phase. The expected result for the unit cell lengths of a=5.8 Å, b=c=10.6 Å, could be refined to a=5.659 Å, b=10.615 Å and c=10.115 Å. Pole figure analysis, using both conventional methods as well as GIXDPF were used to prove that the alignment of the substrate is successfully translated into an alignment of the MOF. The epitaxial order with the MOFs (001) axis parallel to the nanobelt substrates (010) axis and the MOFs (100) axis parallel to the substrates (100) axis can be confirmed.

For the 3-dimensional MOF Cu(BDC)(dabco) no differences were observed, hinting towards its instability in air, leaving Cu(BDC) MOF instead. Freshly prepared samples are needed to do similar analysis for the 3-dimensional MOF as for the 2-dimensional MOF.

The ligand exchange reaction, changing the BDC-linker in Cu(BDC), with an amino-functionalized version of it, did yield unexpected result. An elongation of the linker length of about 50 %, only in the direction perpendicular to the substrate was observed, showing that the ligand exchange reaction in the case of the 2-dimensional Cu(BDC) MOF, induces very significant change in the crystal structure.

12. Bibliography

[1] P. Falcaro, "MOF positioning technology and device fabrication," *Chem. Soc. Rev.*, vol. 43, no. 16, pp. 5513–5560, 2014.

[2] P. Falcaro *et al.*, "Centimetre-scale micropore alignment in oriented polycrystalline metal-organic framework films via heteroepitaxial growth," 2017.

[3] "Metal organic frameworks Industrial Grade." [Online]. Available: https://www.nanoshel.com/metal-organic-frameworks/. [Accessed: 19-Mar-2018].

[4] C. R. Groom, I. J. Bruno, M. P. Lightfoot, and S. C. Ward, "The Cambridge structural database," *Acta Crystallogr. Sect. B Struct. Sci. Cryst. Eng. Mater.*, vol. 72, no. 2, pp. 171–179, 2016.

[5] P. Z. Moghadam *et al.*, "Development of a Cambridge Structural Database Subset: A Collection of Metal-Organic Frameworks for Past, Present, and Future," *Chem. Mater.*, vol. 29, no. 7, pp. 2618–2625, 2017.

[6] M. Savonnet *et al.*, "Combinatorial synthesis of metal–organic frameworks libraries by click-chemistry," *New J. Chem.*, vol. 35, no. 9, p. 1892, 2011.

[7] W. L. Liu, C. Y. Wu, C. Y. Chen, B. Singco, C. H. Lin, and H. Y. Huang, "Fast multipoint immobilized MOF bioreactor," *Chem. - A Eur. J.*, vol. 20, no. 29, pp. 8923–8928, 2014.

[8] N. L. Torad *et al.*, "Direct synthesis of MOF-derived nanoporous carbon with magnetic Co nanoparticles toward efficient water treatment," *Small*, vol. 10, no. 10, pp. 2096–2107, 2014.

[9] J.-H. Wang, M. Li, and D. Li, "A dynamic, luminescent and entangled MOF as a qualitative sensor for volatile organic solvents and a quantitative monitor for acetonitrile vapour," *Chem. Sci.*, vol. 4, no. 4, p. 1793, 2013.

[10] A. Comotti, S. Bracco, T. Ben, S. Qiu, and P. Sozzani, "Molecular rotors in porous organic frameworks," *Angew. Chemie - Int. Ed.*, vol. 53, no. 4, pp. 1043–1047, 2014.

[11] S. Diring *et al.*, "Localized cell stimulation by nitric oxide using a photoactive porous coordination polymer platform," *Nat. Commun.*, vol. 4, pp. 1–8, 2013.

[12] Y. Horiuchi *et al.*, "Visible-light-promoted photocatalytic hydrogen production by using an amino-functionalized Ti(IV) metal-organic framework," *J. Phys. Chem. C*, vol. 116, no. 39, pp. 20848–20853, 2012.

[13] M. Faustini *et al.*, "Microfluidic approach toward continuous and ultrafast synthesis of metal-organic framework crystals and hetero structures in confined microdroplets," *J. Am. Chem. Soc.*, vol. 135, no. 39, pp. 14619–14626, 2013.

[14] H. Hayashi, A. P. Côté, H. Furukawa, M. O'Keeffe, and O. M. Yaghi, "Zeolite A imidazolate frameworks," *Nat. Mater.*, vol. 6, no. 7, pp. 501–506, 2007.

[15] M. Eddaoudi *et al.*, "Systematic Design of Pore Size and Functionality in Isoreticular MOFs and Their Application in Methane Storage Published by : American Association

for the Advancement of Science Linked references are available on JSTOR for this article : Systematic Design," vol. 295, no. 5554, pp. 469–472, 2002.

[16] C. Livage, C. Egger, and G. Férey, "Hybrid Open Networks (MIL 16): Synthesis, Crystal Structure, and Ferrimagnetism of Co 4 (OH) 2 (H 2 O) 2 (C 4 H 4 O 4) 3 ·2H 2 O, a New Layered Cobalt(II) Carboxylate with 14-Membered Ring Channels," *Chem. Mater.*, vol. 11, no. 6, pp. 1546–1550, 1999.

[17] S. S. Y. Chui, S. M. F. Lo, J. P. H. Charmant, a G. Orpen, and I. D. Williams, "A Chemically Functionalizable Nanoporous Material [Cu_3(TMA)_2(H_2O)_3]_n," *Science*, vol. 283, pp. 1148–1150, 1999.

[18] L. Zhao and C. Zhong, "Negative Thermal Expansion in Covalent Organic Framework COF-102," *J. Phys. Chem. C*, vol. 113, no. 39, pp. 16860–16862, 2009.

[19] S. Hausdorf, W. Seichter, E. Weber, and F. O. R. L. Mertens, "Large pores generated by the combination of different inorganic units in a zinc hydroxide ethynylene diisophthalate MOF.," *Dalton Trans.*, no. 7, pp. 1107–13, 2009.

[20] M. Tonigold *et al.*, "Heterogeneous catalytic oxidation by MFU-1: A Cobalt(II)-Containing metal-organic framework," *Angew. Chemie - Int. Ed.*, vol. 48, no. 41, pp. 7546–7550, 2009.

[21] K. M. Ok, J. Sung, G. Hu, R. M. J. Jacobs, and D. O'Hare, "TOF-2: A large 1D channel thorium organic framework," *J. Am. Chem. Soc.*, vol. 130, no. 12, pp. 3762–3763, 2008.

[22] H. Furukawa, K. E. Cordova, M. O'Keeffe, and O. M. Yaghi, "The chemistry and applications of metal-organic frameworks," *Science*, vol. 341, no. 6149, 2013.

[23] D. J. Tranchemontagne, Z. Ni, M. O'Keeffe, and O. M. Yaghi, "Reticular chemistry of metal-organic polyhedra," *Angew. Chemie - Int. Ed.*, vol. 47, no. 28, pp. 5136–5147, 2008.

[24] V. A. Blatov, M. O'Keeffe, and D. M. Proserpio, "Vertex-, face-, point-, Schläfli-, and Delaney-symbols in nets, polyhedra and tilings: recommended terminology," *CrystEngComm*, vol. 12, no. 1, pp. 44–48, 2010.

[25] M. O. Keeffe, M. A. Peskov, S. J. Ramsden, and O. M. Yaghi, "(RCSR) Database of , and Symbols for , Crystal," vol. 41, no. 12, 2008.

[26] M. Li, D. Li, M. O'Keeffe, and O. M. Yaghi, "Topological analysis of metal-organic frameworks with polytopic linkers and/or multiple building units and the minimal transitivity principle," *Chem. Rev.*, vol. 114, no. 2, pp. 1343–1370, 2014.

[27] O. Delgado-Friedrichs and M. O'Keeffe, "Identification of and symmetry computation for crystal nets," *Acta Crystallogr. Sect. A*, vol. 59, no. 4, pp. 351–360, Jul. 2003.

[28] P. Deria, J. E. Mondloch, O. Karagiaridi, W. Bury, J. T. Hupp, and O. K. Farha, "Beyond post-synthesis modification: evolution of metal–organic frameworks via building block replacement," *Chem. Soc. Rev.*, vol. 43, no. 16, pp. 5896–5912, 2014.

[29] S. M. Cohen, "Postsynthetic methods for the functionalization of metal-organic

frameworks," *Chem. Rev.*, vol. 112, no. 2, pp. 970–1000, 2012.

[30] A. F. Gross, E. Sherman, S. L. Mahoney, and J. J. Vajo, "Reversible ligand exchange in a metal-organic framework (MOF): Toward MOF-based dynamic combinatorial chemical systems," *J. Phys. Chem. A*, vol. 117, no. 18, pp. 3771–3776, 2013.

[31] M. Kim, J. F. Cahill, Y. Su, K. A. Prather, and S. M. Cohen, "Postsynthetic ligand exchange as a route to functionalization of 'inert' metal-organic frameworks," *Chem. Sci.*, vol. 3, no. 1, pp. 126–130, 2012.

[32] W. H. Bragg, W. L. Bragg, "The reflection of X-rays by crystals," *Proc. R. Soc. London. Ser. A, Contain. Pap. a Math. Phys. Character*, vol. 88, no. 605, pp. 428–438, 1913.

[33] W. Friedrich, P. Knipping, and M. Laue, "Interferenzerscheinungen bei Röntgenstrahlen," *Ann. Phys.*, vol. 346, no. 10, pp. 971–988, 1913.

[34] R. Resel *et al.*, "Wide-range three-dimensional reciprocal-space mapping: A novel approach applied to organic monodomain thin films," *J. Appl. Crystallogr.*, vol. 40, no. 3, pp. 580–582, 2007.

[35] "Crystallographic planes | Article about Crystallographic planes by The Free Dictionary." [Online]. Available: https://encyclopedia2.thefreedictionary.com/Crystallographic+planes. [Accessed: 19-Mar-2018].

[36] "File:Stereographic projection in 3D.svg - Wikimedia Commons." [Online]. Available: https://commons.wikimedia.org/wiki/File:Stereographic_projection_in_3D.svg. [Accessed: 19-Mar-2018].

[37] "Stereographic projection for cubic crystals." [Online]. Available: http://www.globalsino.com/EM/page4116.html. [Accessed: 19-Mar-2018].

[38] D. J. Robinson, I. K., & Tweet, "No Title," *Rep. Prog. Phys.*, vol. 55, p. 599, 1992.

[39] "XRD1 Beamline Description." [Online]. Available: https://www.elettra.trieste.it/lightsources/elettra/elettra-beamlines/xrd1/xrd1beamlinedescription.html?showall=.

[40] S. Pachmajer and B. Schrode, "GIDVis - a modular MATLAB program to analyze GID images." https://bitbucket.org/s_pachmajer/gidvis, 2018.

[41] H. R. Oswald, A. Reller, H. W. Schmalle, and E. Dubler, "Structure of copper(II) hydroxide, Cu(OH)2," *Acta Crystallogr. Sect. C Cryst. Struct. Commun.*, vol. 46, no. 12, pp. 2279–2284, 1990.

[42] K. Okada *et al.*, "Copper conversion into Cu(OH)2 nanotubes for positioning Cu 3(BTC)2 MOF crystals: Controlling the growth on flat plates, 3D architectures, and as patterns," *Adv. Funct. Mater.*, vol. 24, no. 14, pp. 1969–1977, 2014.

[43] C. Sapsanis *et al.*, "Insights on capacitive interdigitated electrodes coated with MOF thin films: Humidity and VOCs sensing as a case study," *Sensors (Switzerland)*, vol. 15, no. 8, pp. 18153–18166, 2015.

[44] S.-D. Seo, Y.-H. Jin, S.-H. Lee, H.-W. Shim, and D.-W. Kim, "Low-temperature

synthesis of CuO-interlaced nanodiscs for lithium ion battery electrodes.," *Nanoscale Res. Lett.*, vol. 6, no. Ii, p. 397, 2011.

[45]   E. J. SONNEVELD and J. W. VISSER, "Automatic collection of powder data from photographs," *J. Appl. Crystallogr.*, vol. 8, no. 1, pp. 1–7, 1975.

[46]   T. Degen, M. Sadki, E. Bron, U. König, and G. Nénert, "The high score suite," *Powder Diffr.*, vol. 29, no. May, pp. S13–S18, 2014.

[47]   C. F. Macrae *et al.*, "Mercury: Visualization and analysis of crystal structures," *J. Appl. Crystallogr.*, vol. 39, no. 3, pp. 453–457, 2006.

[48]   C. G. Carson *et al.*, "Synthesis and structure characterization of copper terephthalate metal-organic frameworks," *Eur. J. Inorg. Chem.*, no. 16, pp. 2338–2343, 2009.

[49]   C. G. Carson, G. Brunnello, S. G. Lee, S. S. Jang, R. A. Gerhardt, and R. Tannenbaum, "Structure solution from powder diffraction of copper 1,4- benzenedicarboxylate," *Eur. J. Inorg. Chem.*, no. 12, pp. 2140–2145, 2014.

[50]   S. Abdelouhab, M. François, E. Elkaim, and P. Rabu, "Ab initio crystal structure of copper(II) hydroxy-terephthalate by synchrotron powder diffraction and magnetic properties," *Solid State Sci.*, vol. 7, no. 2, pp. 227–232, 2005.

[51]   I. Salzmann and R. Resel, "STEREOPOLE: Software for the analysis of X-ray diffraction pole figures with IDL," *J. Appl. Crystallogr.*, vol. 37, no. 6, pp. 1029–1033, 2004.